

Fully Integrated Fluorescence Biosensors On-Chip Employing Multi-Functional Nanoplasmonic Optical Structures in CMOS

Lingyu Hong, Hao Li, Haw Yang, and Kaushik Sengupta, *Member, IEEE*

Abstract—Integrated optical system-on-chip in silicon operating in the visible range can have a tremendous impact on enabling new applications in sensing and imaging through the ultra-miniaturization of complex optical instrumentation. CMOS technology has allowed an integration of optical detection circuitry for image sensors with massively large number of pixels. In this paper, we focus on techniques to realize complex optical-field processing elements inside CMOS by exploiting optical interaction with sub-wavelength metal nanostructures realized in the electrical interconnects layers, whose feature sizes are now in the sub-100-nm range. In particular, we present a fully integrated fluorescence-based bio-molecular sensor in 65-nm CMOS with integrated nanoplasmonic waveguide-based filters capable of more than 50 dB of rejection ratio across a wide range of incident angles. Co-designed with the integrated photo-detection circuitry, capacitive TIAs, and correlated double-sampling circuitry, the sensor is capable of detecting 48 zeptomoles of quantum dots on the surface with 52 fA of photodetector current with a fluorescence/excitation ratio of nearly -62 dB without any post-fabrication, external optical filters, lenses, or collimators. The ability to integrate complex nanoplasmonic metal structures with unique optical properties in CMOS with no post-processing creates the opportunity to enable large multiplexed assays on a single chip and a wide variety of applications, from *in vitro* to *in vivo*.

Index Terms—Biochips, biosensor, CMOS, CMOS imager, fluorescence, metal optics, microarray, nano-optics, nanoplasmonics, spectroscopy.

I. INTRODUCTION

INTEGRATED, low-cost, and portable point-of-care diagnostic technology has the potential to bring transformative changes in healthcare. In recent past, there have been considerable research efforts aiming to exploit the integration capability of IC technology, especially CMOS, to realize fully integrated, low-cost, portable, affinity-based bio-sensing platforms, such as for proteomic or nucleic acid assays [1]–[5]. The detection methodology for an affinity-based biosensor platform relies on the selective capture of target bio-molecules by capture probes, and the chemistry is transduced either label-free using methods such as impedance spectroscopy,

Manuscript received June 14, 2016; revised January 13, 2017 and April 8, 2017; accepted May 29, 2017. Date of publication July 18, 2017; date of current version August 22, 2017. This paper was approved by Associate Editor Michiel A. P. Pertijis. (*Corresponding author: Kaushik Sengupta*)

L. Hong and K. Sengupta are with the Integrated Microsystems Research Laboratory, Department of Electrical Engineering, Princeton University, Princeton, NJ 08544 USA (e-mail: lingyu@princeton.edu).

H. Li and H. Yang are with the Haw Yang Laboratory, Department of Chemistry, Princeton University, Princeton, NJ 08544 USA.

Color versions of one or more of the figures in this paper are available online at <http://ieeexplore.ieee.org>.

Digital Object Identifier 10.1109/JSSC.2017.2712612

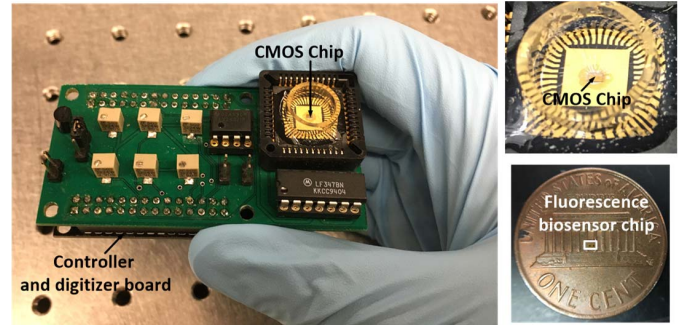


Fig. 1. Single-chip fluorescence-based biosensor with integrated nanoplasmonic filters in 65-nm CMOS.

dielectric changes, electro-chemical [6]–[8], and Raman scattering or with labels such as magnetic [9]–[13] and fluorescence [14]–[29]. Each label or reporter molecule causes some change in the electromagnetic (EM) environment in the vicinity of the sensing platform (chip), and the electronic circuitry is designed to measure such changes with high sensitivity. While processing low-frequency fields due to magnetic labels or dielectric labels are well known with ICs [6]–[13], affinity-based fluorescence sensing is the most adopted as well as sensitive, specific, and robust sensing modality in diagnostic and in medical research [14]. However, such fluorescence sensing often requires a multitude of external optical elements such as lenses, objectives, thin film or dichroic filters, charge-coupled device or photo-multiplier tube (PMT) detectors, precision mechanical scanners, all of which make the system complex, bulky, and expensive. In the absence of high-performance integrated optical components, miniaturization of a fluorescence sensing system in CMOS has relied on externally grown optical filters and/or collimators [15], [18], [20], or time-resolved techniques with synchronized sources [16], [17], [19], [22], [23], which require very high-speed and moderately high-power driving circuitry, sub-ns timing accuracy, and low-noise photo-detection capability. This can add significant cost, size, and complexity to the system, preventing many applications where miniaturization is the key.

In this paper, we discuss the methods by which optical-field manipulation can be achieved in standard CMOS technology exploiting sub-wavelength interaction of metal-optic nanostructures with incident optical fields in the visible range. The underpinning concept behind this work is that in addition to active device scaling which has allowed integration of nano-scale devices with increasing high performance, simultaneous

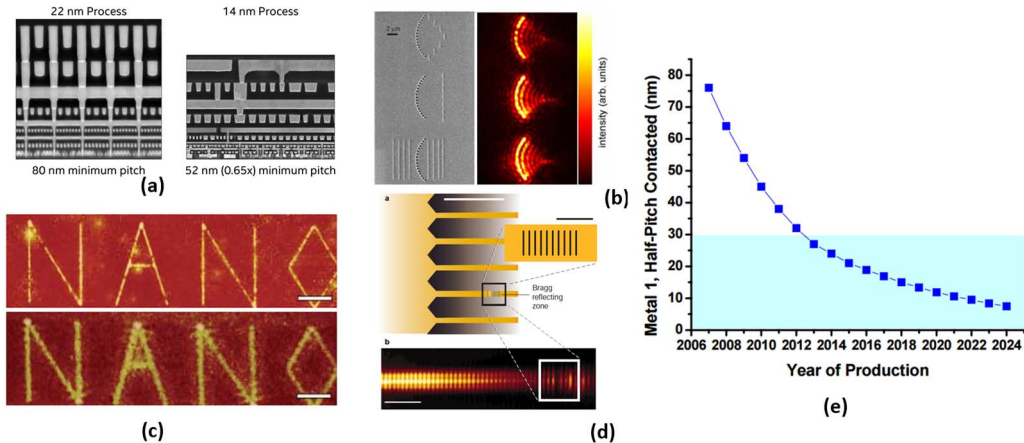


Fig. 2. Sub-wavelength interaction of light and metal nanostructures. (a) SEM cross sections of 22- and 14-nm technology nodes demonstrating lithographic scaling [30]. Examples of nanoplasmonic structures and functionalities (b) Nano-optic lensing [41], (c) Sub-diffraction imaging [35], and (d) Nano Bragg-reflector gratings [40]. (e) Sub-100-nm lithographic features in state-of-the-art silicon IC processes which create opportunities for copper-based complex nanoplasmonic multi-functional optical components [32].

interconnect scaling has led to the possibility of metal nanostructures with lithographic features of 100 nm and below in the deep sub-wavelength regime at optical frequencies [30]–[32]. Traditionally, these copper-based interconnects have been used to allow electronic information flow across devices, but they can simultaneously be exploited to interact with optical fields inside the chip creating complex, multi-functional optical elements [29]. We show, for the first time, the ability to incorporate 3-D-nanoplasmonic structures in standard CMOS by exploiting the sub-wavelength copper-based electrical interconnect lithography features for fully integrated optical SOCs in the visible range. Fig. 1 shows the fluorescence-based CMOS biosensor with integrated nanoplasmonic filters realized in a 65-nm process, which encompasses the assay platform, sensor, and read-out circuitry all integrated in a single chip, eliminating the need for any post-fabrication or external optical elements, except for an inexpensive excitation source (a continuous-wave diode laser or LED). As a biosensor, it has the capability of detecting 48 zeptomoles (48×10^{-21} mol) of quantum-dot (Qdot)-based fluorescence labels on the chip surface, higher than many current microplate readers [33]. This paper presents a nanophotonic-electronic co-design approach toward fully integrated fluorescence biosensor with on-chip copper-based nanoplasmonic filters.

Nano-plasmonics is the study of interaction of optical fields with metallic nanostructures [34] and has made tremendous progress in recent years for its ability to confine, concentrate, guide, and filter light with nano-scale noble metals, opening up many exciting applications including deep sub-diffraction imaging [35], significant fluorescence spectroscopy signal enhancement [36], sub-wavelength optical wave-guiding with extreme mode confinement [37], extraordinary optical transmission through sub-wavelength hole arrays [38], and perfect lensing [39]–[41], as shown in Fig. 2(a)–(d). The ability to incorporate flat optical components in a CMOS process through this sub-wavelength metal lithographic features [Fig. 2(e)] can lead to a new class of complex, ultra-miniaturized, low-power sensing and imaging systems manufacturable in a scalable fashion [42]–[46].

This paper is organized as follows. Section II presents the overview of a fluorescence-based biosensor to allow us to understand the optical and electronic specifications for the chip-scale platform. Section III reviews the fundamental principles of nano-plasmonics and sub-wavelength field confinement in metallic nanostructures in CMOS which is the principle behind the operation of the integrated optical filters. Section IV discusses the electronic-nanophotonic co-design techniques for the chip. Section V presents the sensor architecture, and Section VI discusses the measurement results. Analysis of limit of detection (LOD) and its dependence on noise and system parameters is presented in the Appendix.

II. FLUORESCENCE-BASED BIO-ASSAYS: SYSTEM OVERVIEW

A. Optical Filtering Requirements

In the fluorescence-based affinity sensing, target molecules are allowed to interact with immobilized capture probes on a glass substrate and secondary capture molecules with fluorescence labels provide the transduction information into optically detectable signals (Fig. 3), often in a spatially multiplexed architecture. While the specificity of the assay is related to the binding affinity, the key toward sensitive detection is to distinguish a very weak fluorescence signal from the background excitation light. Once the assay is completed, a thin film of fluorescence labels of concentration (C) and of thickness (l) on the surface will absorb a fraction of the excitation light (P_{ex}) given by $P_{\text{abs}} = P_{\text{ex}}(1 - e^{-\alpha_{\text{abs}}Cl})$, where P_{abs} is the absorbed light and α_{abs} is the molar extinction coefficient. In this work, Qdots have been chosen as the preferred labeling agent for their photo-stability, stronger emission, and higher Stokes shift [47]. Therefore, for the particular label Qdot 800 [48] with $A_{\text{qdot}} = 1.76 \text{ nm}^2$, a fractional coverage area of 1.76×10^{-6} by the Qdots needs to be detected for surface-sensitivities approaching $1\text{dot}/\mu\text{m}^2$ (~ 16.6 zeptomoles for a $100 \mu\text{m} \times 100 \mu\text{m}$ sensor). This implies that out of 10^7 excitation photons, only four photons of fluorescence signal will emerge for a quantum efficiency of 0.25. Detecting the fluorescence signal, therefore, requires

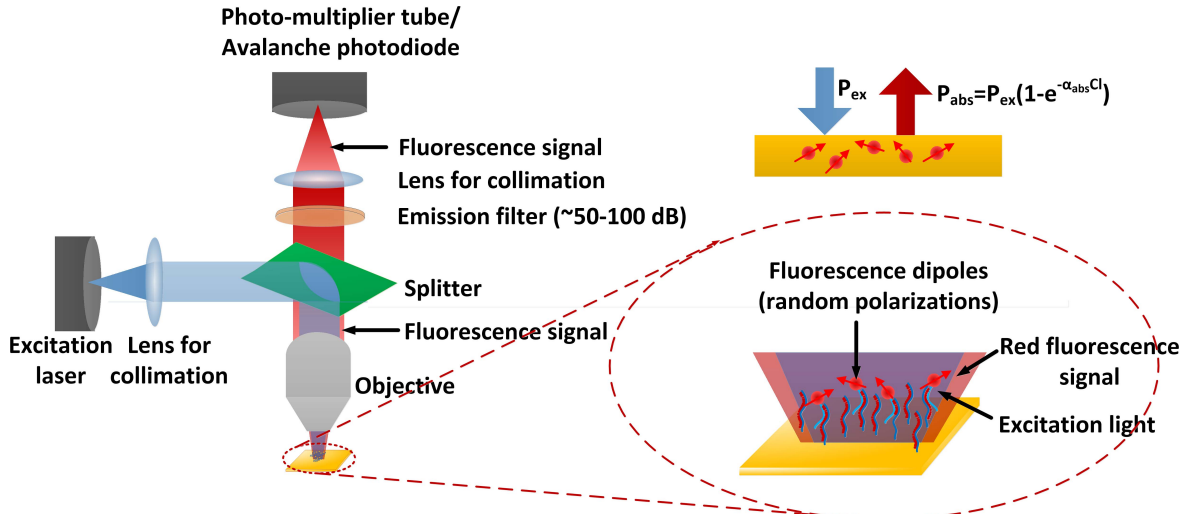


Fig. 3. Typical fluorescence-based optical biosensing setup requires collimated optics and multi-layer interference-based filters with 50–100 dB of excitation rejection for sensitive assays. Light is captured by avalanche photodiodes or photo-multiplier tubes and the entire setup is tightly shielded from stray light.

net rejection/extinction ratio on the order of 60 dB. This is achieved in a traditional fluorescence sensing system with multiple multi-layer interference-based filters (Fig. 3) or with back-illumination separating the excitation and fluorescence paths. Being able to remove the external optical components and miniaturize complex, multiplexed biosensors into a single chip can not only reduce cost and system size, but also potentially enable new applications *in vivo* and *in vitro*, from handheld diagnostic devices for infectious diseases to *in vivo* sensing of biochemical markers for real-time monitoring. The ability to integrate millions of pixels in a single chip indicates that CMOS is an excellent platform for multiplexed detection. However, the integrated optical filters inside the chip to detect the fluorophores on the surface need to satisfy various optical properties. As shown in Fig. 4, the immobilized fluorescence tags on the chip surface directly couple light into the chip, which gets filtered on-chip, and then detected and processed electronically in the dual-sensing architecture.

B. Chip-Scale Implementation

Ever since the discovery of extraordinary optical transmission through sub-wavelength hole arrays [38], numerous works have been reported on surface-plasmon-based nanostructured metallic thin films that control spectral responses of optical transmission [39]–[42], [49]–[59]. This includes nanostructured metallic thin films deposited on image sensors functioning as red-green-blue (RGB) filters [58], [59]. However, the extinction ratio required for sensitive optical bioassays is the orders of magnitude higher, and therefore needs to be based on fundamentally different physical principles as elaborated in the following sections. Unlike collimated light in [58] and [59], the Qdots on the surface (Fig. 4) act as optical dipoles oriented at random polarizations and radiating at random angles of incidence coupling to the chip. This requires the filter to be very robust to angle and process variations, neither of which can be achieved by the resonant plasmonic structures such as those in [58] and [59]. Moreover, the post-fabrication process for the deposition of metallic thin films on CMOS sensors suffers from significant additional

cost and from the lack of precision lithographical alignment. In addition, extremely robust optical shielding (greater than 60 dB) must be incorporated to prevent any stray light leakage which is more readily achievable with monolithic integration of the filters. The lithographic fabrication techniques in CMOS allow the integration of nanoplasmonic structures with high aspect ratios which is exploited in this paper to realize vertical waveguides transporting coupled surface-plasmon polariton (SPP) modes. While as a proof of concept, we demonstrate a dual-sensing architecture, this can be scaled to a large multiplexed array (~ 1000 s) for parallel detection of multiple analytes simultaneously with shared read-out circuitry and a shared nanoplasmonic filter sheet spread across the chip surface.

III. NANOPLASMONICS: INTERACTION OF LIGHT WITH METAL NANOSTRUCTURES

A. Review of Plasmonics

Metals interact with EM fields at optical frequencies very differently than they do at radio frequencies due to the finite response time of electrons. When an impulse EM wave is incident on a metal surface, the dynamics of the electron gas in the metal needs to be considered. For a time-harmonic field, the relative dielectric constant of metal $\varepsilon(\omega)$ captures the dynamics from RF to optical frequencies and can be expressed in the form of the Drude's model

$$\varepsilon(\omega) = 1 - \frac{\omega_p^2}{\omega^2 + i\gamma\omega} \quad (1)$$

where ω_p is the bulk plasma frequency of the free electron gas in the metal. For copper, f_p (≈ 2000 THz) falls in UV region corresponding to $\lambda_p \approx 155$ nm. Expressing $\varepsilon(\omega) = \varepsilon_1(\omega) + i\varepsilon_2(\omega)$, we have $\varepsilon_1(\omega) = 1 - ((\omega_p^2)/(\omega^2 + \gamma^2))$, $\varepsilon_2(\omega) = ((\omega_p^2\gamma)/(\omega(\omega^2 + \gamma^2)))$. At radio frequencies ($\omega \ll \gamma$), $\varepsilon(\omega) \approx i\varepsilon_2(\omega)$ which leads to significant absorbing characteristics of metal given by the well-known absorption coefficient at low frequencies as

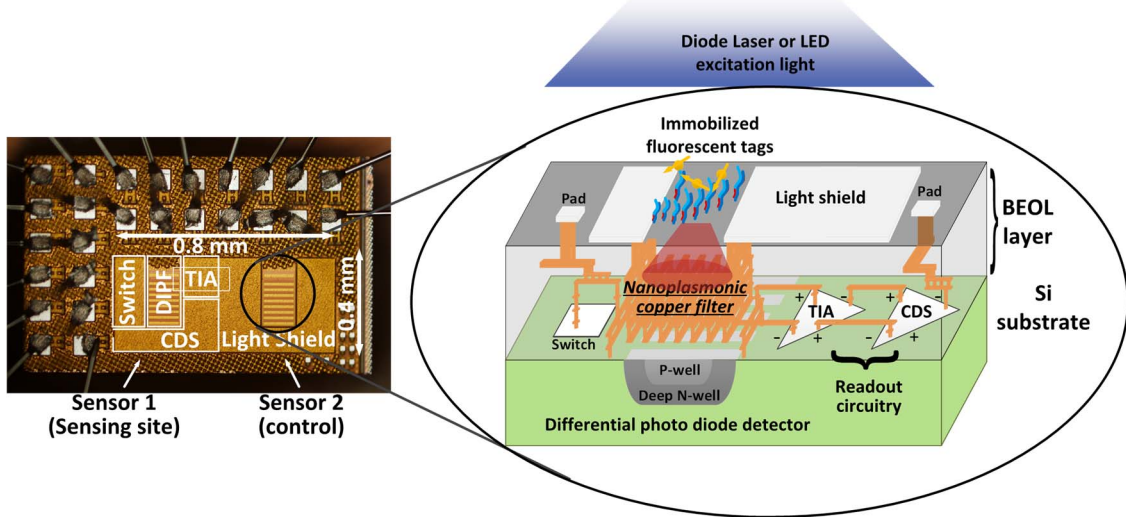


Fig. 4. Chip micrograph of the CMOS-based fluorescence sensor with dual-sensing sites and integrated nanoplasmonic filter. When excited, the Qdots fluorescence as random dipoles radiating mostly into the chip to be detected and processed differentially with a reference optically shielded diode, while the nanoplasmonic filter blocks the excitation laser.

$\alpha(\omega) = \text{Im}[\omega\sqrt{\mu_0\epsilon_0\epsilon(\omega)}] = \sqrt{\frac{\omega_p^2\omega}{2\gamma c^2}} = \sqrt{\frac{\mu_0\omega\sigma_0}{2}}$.¹ However, for much higher frequencies in the near-infrared (NIR) range ($\omega \gg \gamma \approx 20$ THz for copper), the damping effect decreases and the dielectric constant can be approximated by

$$\epsilon(\omega) \approx \epsilon_1(\omega) = 1 - \frac{\omega_p^2}{\omega^2}. \quad (2)$$

Fig. 5 illustrates the qualitative behavior of materials with refractive index $n = (\mu\epsilon/(\mu_0\epsilon_0))^{1/2}$ for varying ϵ and μ . As shown in Fig. 5, $\epsilon(\omega) = 0$ at $\omega = \omega_p$ and for $\omega < \omega_p$, metals behave as electrical plasma with $\text{Re}(\epsilon(\omega)) < 0$ which is key toward understanding sub-wavelength field confinement in propagating SPPs.²

B. Confinement of Optical Fields in Nano-Scale: Surface-Plasmon Polaritons on Copper in CMOS

SPPs are EM waves which arise due to coupling of the EM field to oscillating electrons in the metal and propagate at the interface between dielectric (ϵ_d) and metal (ϵ_m) with exponentially decaying fields in both media. While the modal analysis of SPP is beyond the scope of this paper, it can be shown that SPP propagates at the interface of two materials when the following conditions satisfy, namely, $\text{Re}(\epsilon_m) < 0$ and $\epsilon_d > 0$ [34] which holds true for the metal–dielectric interface for frequencies $\omega < \omega_p$. In addition, the dispersion relation for the SPP mode can be shown to satisfy

$$k_{\text{spp}} = k_0 \sqrt{\frac{\epsilon_m \epsilon_d}{\epsilon_m + \epsilon_d}} \quad (3)$$

where k_{spp} and k_0 denote the wave vectors of the SPP mode and free-space air mode, respectively. As the frequency approaches the value where $\epsilon_m(\omega) + \epsilon_d(\omega) = 0$,

¹This is the region of operation where the skin depth δ is of the known form $\delta = (1/\alpha) = (2/(\mu_0\omega\sigma_0))^{1/2}$

²At even higher frequencies extending from NIR to visible, the photon energy can cause inter-band transition of electrons leading to excess losses and therefore, a higher imaginary component in $\epsilon(\omega)$.

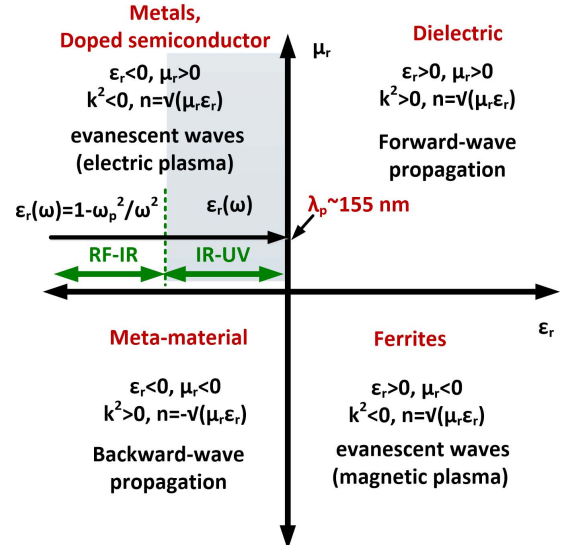


Fig. 5. Behavior of materials with varying ϵ and μ . Metals lie in the portion of the plot with $\text{Re}(\epsilon(\omega)) < 0$ for $\omega < \omega_p$ and $\text{Re}(\epsilon(\omega)) = 0$ at $\omega = \omega_p$, where ω_p is the bulk plasmon resonance frequency. ω_p for copper lies in the UV region corresponding to $\lambda_p = 155$ nm [55].

an SPP mode develops with $k_{\text{spp}} \rightarrow \infty$ and group velocity $v_g \rightarrow 0$ for ideal metal. For real metals with losses, bound SPPs approach a small but finite SPP wavelength $\lambda_{\text{spp}}(\omega) = (2\pi/(\text{Re}[k_{\text{spp}}]))$ with characteristic propagation length of $\delta_{\text{spp}}(\omega) = (1/(\text{Im}[k_{\text{spp}}]))$. This frequency-dependent loss of copper is exploited for robust and non-resonant on-chip filtering through the vertical propagation of coupled SPP from the chip surface to the photodetectors.

C. Copper as a Plasmonic Material

Fig. 6 shows both real and imaginary dielectric constant of copper against frequency and compared with gold, a standard plasmonic material. Fig. 6 indicates that copper can be exploited in CMOS as a good plasmonic material at

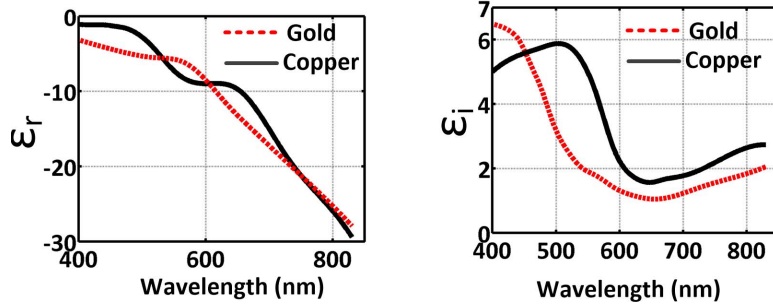


Fig. 6. Dielectric constant (real and imaginary parts) of copper in the visible range [55].

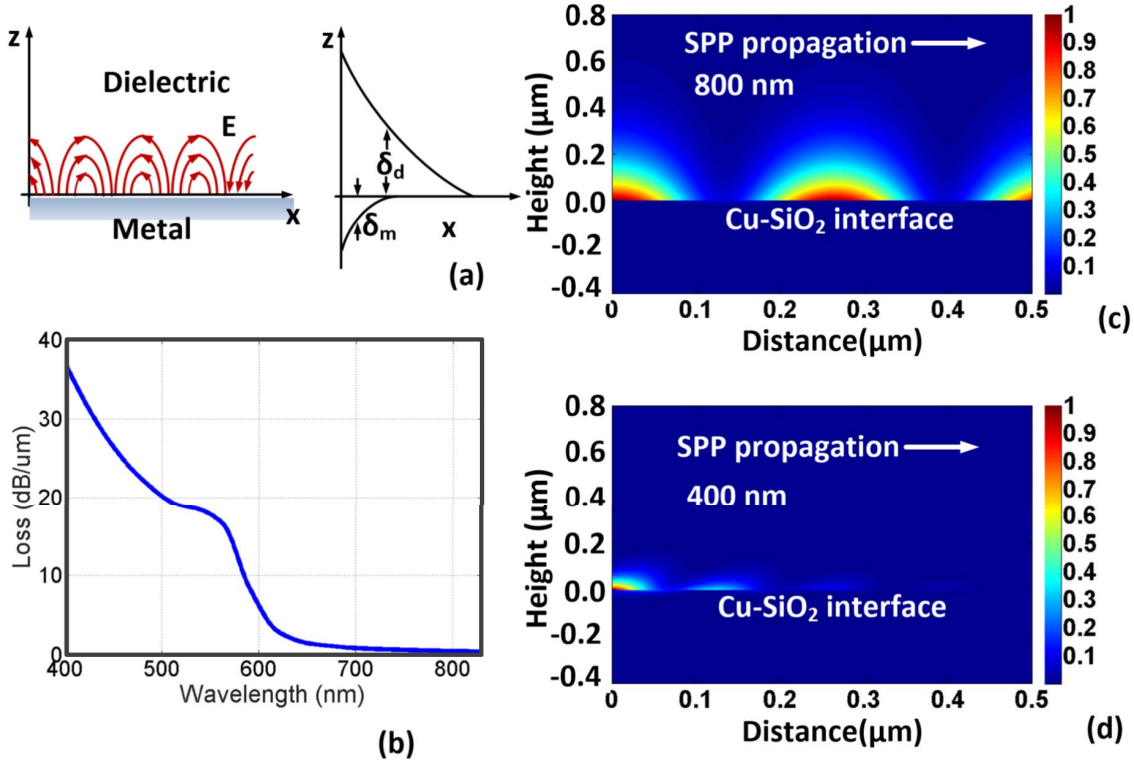


Fig. 7. (a) Propagation of SPPs on the surface of a metal–dielectric interface. (b) Propagation loss for SPP at Cu–SiO₂ interface showing nearly 35 dB/μm difference between 400 and 800 nm. This is the key to the operation of the robust integrated nanoplasmonic filter. Electric field of SPP propagation at Cu–SiO₂ interface for (c) 800- and (d) 405-nm wavelengths, respectively, showing the difference in propagation loss over 0.5 μm.

long wavelengths (below NIR frequency), while its much higher loss at shorter wavelengths (near 500 nm) can also be exploited as a spectral filtering mechanism for propagating SPPs [Fig. 7(a)]. Fig. 7(b) shows the analytically calculated loss of SPP propagation in dB/μm at planar and laterally infinite Cu–SiO₂ interface. The calculation was carried by imposing the boundary conditions of the interface and the dielectric constants for copper and SiO₂ in these wavelength regimes. Fig. 7 demonstrates that nearly 70 dB of filtering ratio is achievable between 400 and 800 nm for a 2-μm wave travel. This is clearly seen in the analytical calculations in Fig. 7(c) and (d) capturing the exponential field decay for SPPs at 800 and 400 nm, respectively. This principle is exploited to enable background suppression with vertical nanoplasmonic waveguides, as shown in Fig. 4.

IV. CMOS NANOPHOTONIC-ELECTRONIC CO-DESIGN

A. Nanophotonic Filter Design and Realization in CMOS

The vertically propagating SPP-based waveguide is realized as a periodic array with sub-wavelength spacing using the lowest five Cu layers (M₁–M₅) in a bulk 65-nm CMOS process. The details of the integrated filter are shown in Fig. 8. Several variants of the filter ranging from the lowest three to five layers with vertical lengths ranging from 1 to 1.77 μm were fabricated and tested. In order to comply with the foundry Design-rule-check (DRC) rules, the widths of the metals and the vias are kept minimum at 100 nm and spaced at 130 nm. The array supports coupled SPP modes, and spectral filtering is achieved non-resonantly by exploiting different losses for different wavelengths. The finite-difference time-domain (FDTD) EM

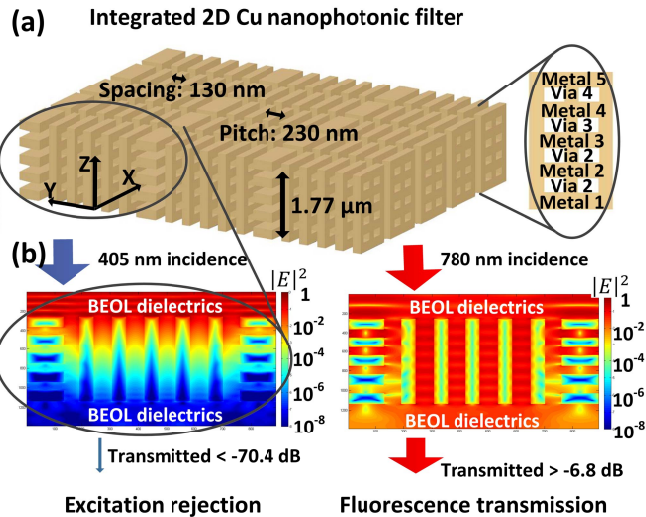


Fig. 8. (a) Cross section of the integrated 3-D nanoplasmonic filter realized with copper-based bottom five metal layers and four via layers. (b) FDTD simulations of the filters show extinction ratio of the order 63 dB with polarization in the y-direction.

simulation of the field in the waveguide array in Fig. 8 shows that the fluorescence signal near 780 nm is transmitted with a loss of 7 dB, while the excitation at 405 nm is suppressed by more than 70 dB with a rejection ratio of more than 63 dB. It will be shown later that the rejection ratio primarily determines the sensor's LOD under typical background limited conditions. A detailed modal analysis is beyond the scope of this paper, but the sub-wavelength spacing of the design cuts off other cavity modes, except the coupled SPP modes.

B. Filter Performance, Polarization, and Scaling

The integrated filters can be designed as 1-D or 2-D waveguide array for single or dual polarization operation, respectively. As shown in the simulated spectral performance in Fig. 9(a), the asymmetry of the performance in the two polarizations is due to compliance with minimal metal-area DRC rule on each element that leads to an asymmetry in the design element. Fig. 9(b) illustrates the variation of the filter performance with spacing and linewidth and shows that rejection ratio improves with down-scaling in all lateral dimensions. Deep sub-wavelength dimensions ensure the dominance of coupled SPP modes and stronger suppression of all the other cavity modes. With increased spacing, partial leakage of the evanescently coupled TE modes reduces the rejection ratio. As an example, for 32-nm CMOS process with 65-nm spacing and 50-nm linewidths, 70–80 dB of filtering ratio can be achieved. This can almost completely eliminate background and improve the sensor's LOD by more than two orders of magnitude approaching single-molecule level.

C. Filter Robustness to Angle of Incidence, Lithography, and Process Variations

As discussed before, in the absence of collimation, the performance of the filter needs to be evaluated with exci-

tation from randomly oriented fluorescence dipoles on the surface of the chip. Fig. 10 illustrates that randomly polarized electric dipoles at the interface between air and SiO₂ couple majority of its radiation into the chip, though not at broadside [61], [62]. Since the filter is not based on interference but propagation loss, its rejection ratio is robust against angle of incidence, polarization, and process variations. Fig. 11(a) shows the simulated transmission spectrum for oblique plane-wave incidence ranging from 0° to 40°. Fig. 11(b) also shows the comparison of simulated transmission spectrum for regular-shaped planar waveguides against CMOS lithography-compatible waveguides with angular walls. In addition, the filter performance is simulated for lithographic variations modeled by the Gaussian distribution of metal linewidths and spacings [Fig. 12(a)]. In order to capture the filter performance against stray and scattered laser light, Monte Carlo simulation using dipole clouds with random orientations, polarizations, and positions are employed as the input source, as shown in Fig. 12(b). The filter performance preserves well in all cases.

D. CMOS Compatibility and Electronic-Circuit Co-Simulation

To ensure CMOS compatibility and prevent stray light leakage, the nano-optic structures are co-designed with the metal interconnects for electrical routing. In addition, the accuracy of EM simulation for nano-optic structures can be compromised by the lack of exact information of various material properties such as the exact composite of the Cu interconnects, barrier diffusion layers, and the surrounding low-K dielectrics. Also, to reduce computation time, regular and modular structures can enable segmentation and ease of simulation as unit cells with periodic boundary conditions. An FDTD-based simulation software is used to analyze the copper-based nano-optic structures surrounded by a homogenous silicon dioxide. The results are combined with circuit and system simulations.

V. SENSOR CIRCUITRY AND ARCHITECTURE

Fig. 13 illustrates the sensor architecture which shows the sensing modality with a sensing site (Sensor 1) and a control site (Sensor 2). This allows laser light leakage into the sensors to appear as common-mode perturbation and to be suppressed electronically down the chain, achieving a net background suppression of orders of magnitude higher than what can be achieved purely optically. Each sensing site comprises of a differential photodiode with inter-laid fingers to minimize the differential dark current. The individual dark currents appear as common mode which are then suppressed electronically through differential circuits. The differential signal is amplified by a capacitive trans-impedance amplifier (CTIA), and is processed through a differential correlated double-sampling (CDS) circuit to suppress offsets and low-frequency correlated noise [66]. The signals are finally acquired by a 12-b data acquisition and digitizer board.

A. Common-Mode Dark Current Suppression

In the absence of custom foundry models for the photodiodes, the architecture needs to be robust to dark current

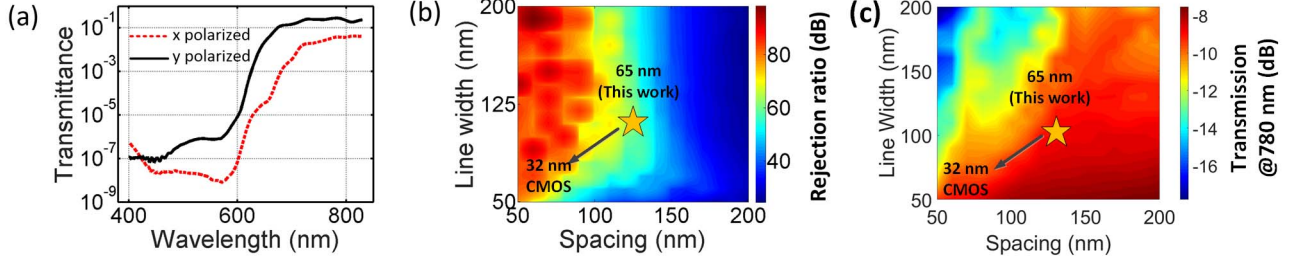


Fig. 9. (a) Simulated performance of the integrated nanoplasmonic filter for both polarizations. The asymmetry is due to the asymmetry in the dimensions of a single element where one side is kept at a minimal feature length and the other side kept slightly longer to comply with the minimum area requirement of a stand-alone metal element. (b) Extinction ratio improves with scaling, reaching toward 70–80 dB of rejection for 65-nm spacing and 50-nm linewidths. (c) Simulated transmission losses at the fluorescence wavelengths range between 7 and 9 dB and remain similar as we scale toward the 32-nm CMOS process.

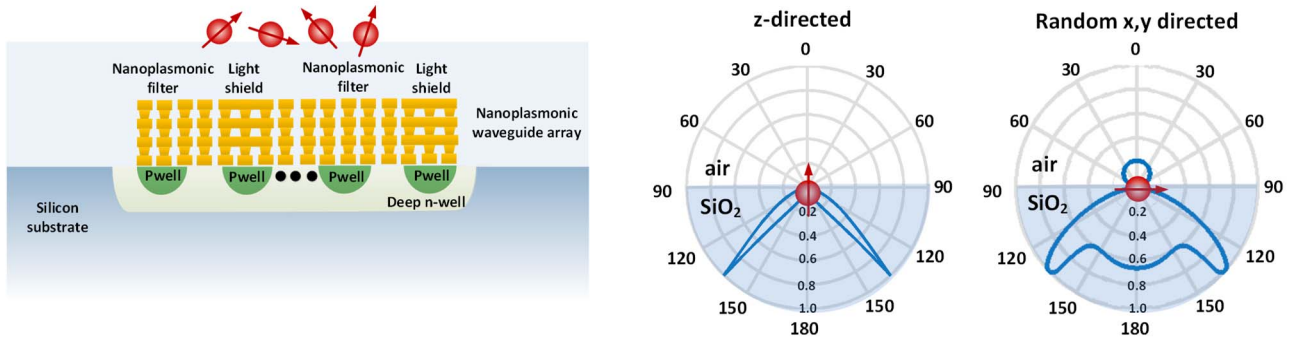


Fig. 10. Optical radiation profile of fluorescence labels can be modeled as dipoles at the interface between silicon dioxide and air. The figure shows the emission profile of z-directed fluorescence dipole and average radiation profile of randomly oriented xy dipoles at the interface between air and dielectric. The profile demonstrates that most of the emission power gets coupled to the dielectric and on to the integrated filter.

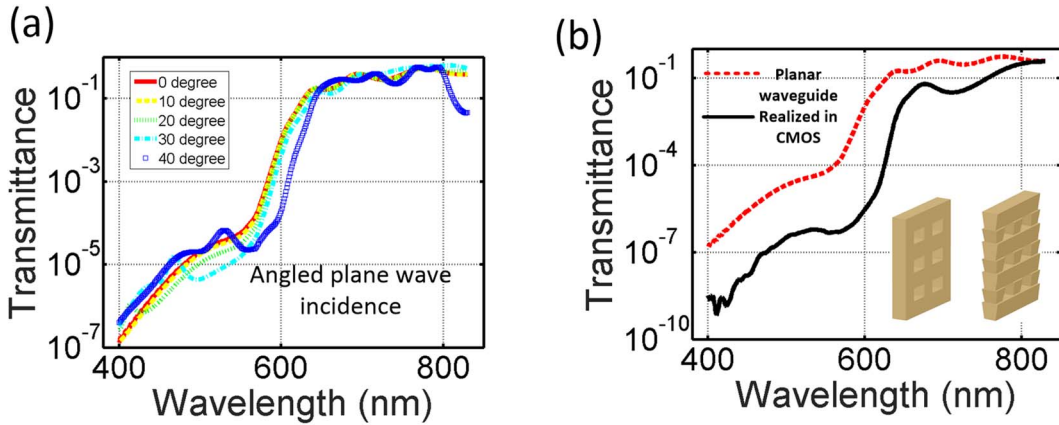


Fig. 11. (a) Simulated performance of the integrated nanoplasmonic filter demonstrating robustness against angle of incidence (b) Spectral responsivity of the filter with non-planar sidewalls with 10° angle, typical for a CMOS-implemented designs.

which can otherwise overwhelm the photocurrent, and therefore reduce the integration time and sensitivity. As a first measure shown in Fig. 13, dark current is suppressed with two photodiodes laid out alternatively covered by integrated filter and metal shield, respectively. The interdigitated layout ensures a good matching between the diodes allowing partial suppression of the common-mode dark current.

B. Photodiodes Structures

Four different photodiode structures (D_1 – D_4) are designed, fabricated, and measured, as shown in Fig. 14(a)–(d). D_1 and D_2 utilize p-n junctions at the interface of n-well and

p-substrate with different sizes of n⁺ contact area to collect photoelectrons. D_3 achieves the same in the depletion well between p-well and deep n-wells, typically used for triple well transistors. D_4 uses the pn-junction between p-well and n⁺ active region inside the isolation deep n-well. The interdigitated layout of the sensing diode along with the shielded reference diode is shown in Fig. 14(e). The responsivity for D_1 and D_3 at 780 nm was measured to be 0.022 A/W, almost 2–3 times higher than that for D_2 and D_4 [Fig. 14(f)]³.

³In calculation of diode responsivity, only the light power impinging on the sensor diode area (and not the reference diode) is taken into consideration.

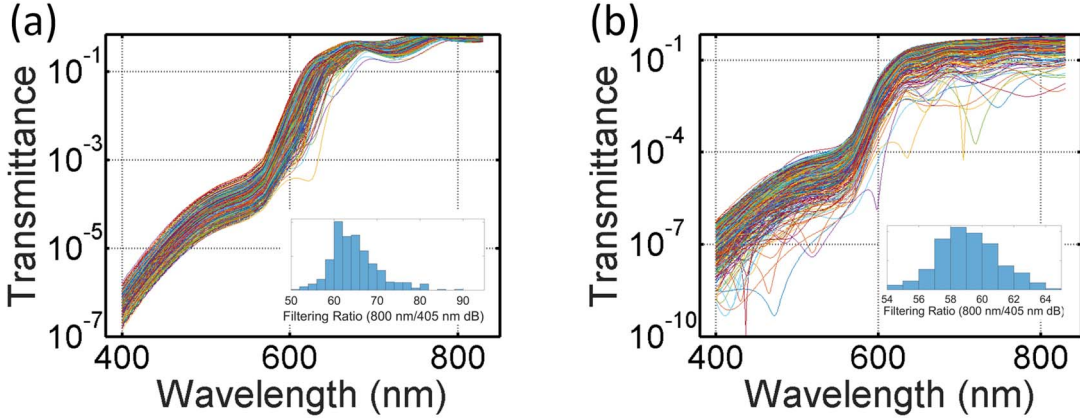


Fig. 12. Simulated performance of the filter against (a) process variations ($3\sigma = 20$ nm) for normal incidence and (b) random polarizations of the dipole clouds on the chip surface. Non-resonant nature of the SPP-based filter is the primary reason for its robustness against fabrication tolerances and orientation of the excitation dipoles.

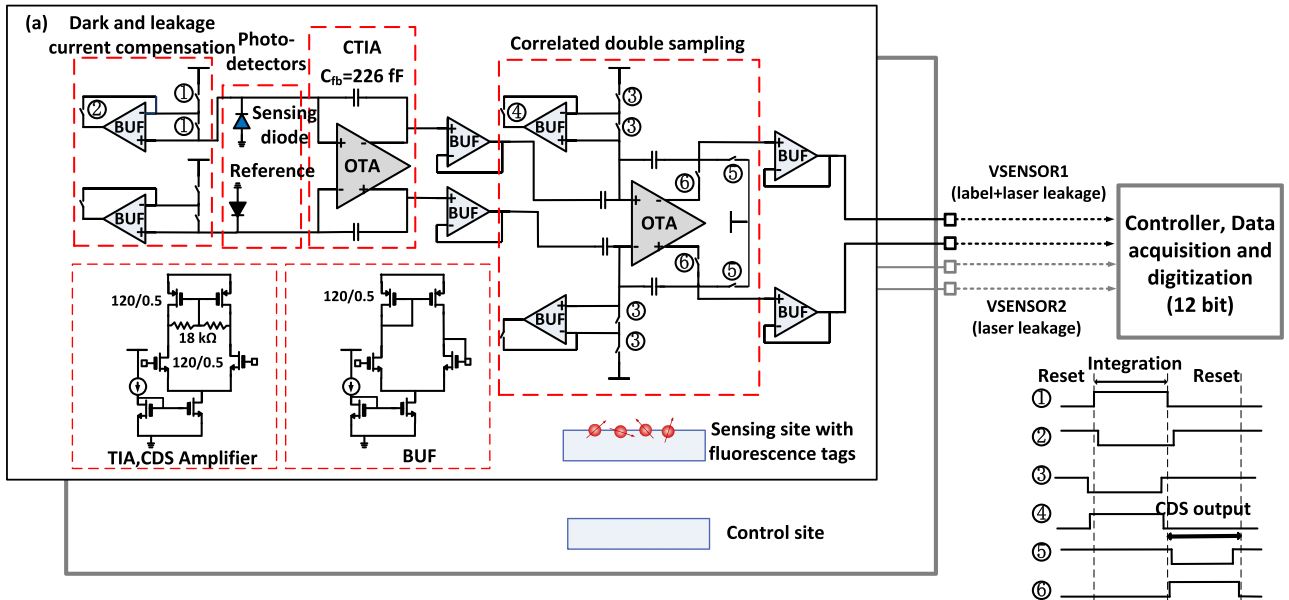


Fig. 13. Photo-detection circuitry showing differential sensing and correlated double-sampling architecture and the off-chip interface. The figure also shows a timing diagram for the control circuits.

This is attributed to the higher optical absorption in the highly doped active regions and shallow depletion regions of the photodiodes. This measurement includes effects of all optical losses, reflections from dielectric interfaces, and moderately low quantum efficiencies of the diodes realized in a bulk digital CMOS process. For the rest of this paper, the diode used in measurement is D_3 in Fig. 14.

C. Leakage, Dark Current Suppression and CTIA

In order to sense femto-watt level of fluorescence light in the absence of accurate photodiode models, effects of dark and leakage currents need to be carefully considered. This is illustrated in Fig. 15. If the dark current and the photodiode reverse-bias current together are of the same order as the total switch leakage current, they can partially compensate each other. If the leakage current is dominant, a feedback circuitry using a buffer can be enabled

through S_2 equalizing the drain-source voltages of the PMOS switch and significantly suppressing the subthreshold leakage through the PMOS switch S_1 ($I_{\text{leak}1}$) and the reverse-biased diode in the drain n-well junction ($I_{\text{leak}2}$) (Fig. 15). As shown in Fig. 13, this architecture was implemented four times in each sensor for the control switches in the sensing diode, the reference diode, and the differential CDS circuit. The photo current is integrated in a CTIA, as $V_{\text{op,TIA}} = \int ((i_{\text{ph}}(t))/(C_{\text{fb}}(1 + (1/A)) + (C_d/A)))dt \approx \int ((i_{\text{ph}}(t))/C_{\text{fb}})dt$ where $C_{\text{fb}} = 226$ fF is the feedback capacitance, A is the amplifier gain (≈ 32.7 dB), and C_d is the diode capacitance whose effect is significantly reduced [63].

D. Correlated Double-Sampling Architecture

The signal at the output of the CTIA is processed by differential CDS circuits to suppress offset and correlated 1/f noise. As shown in Fig. 16, the CDS captures the difference

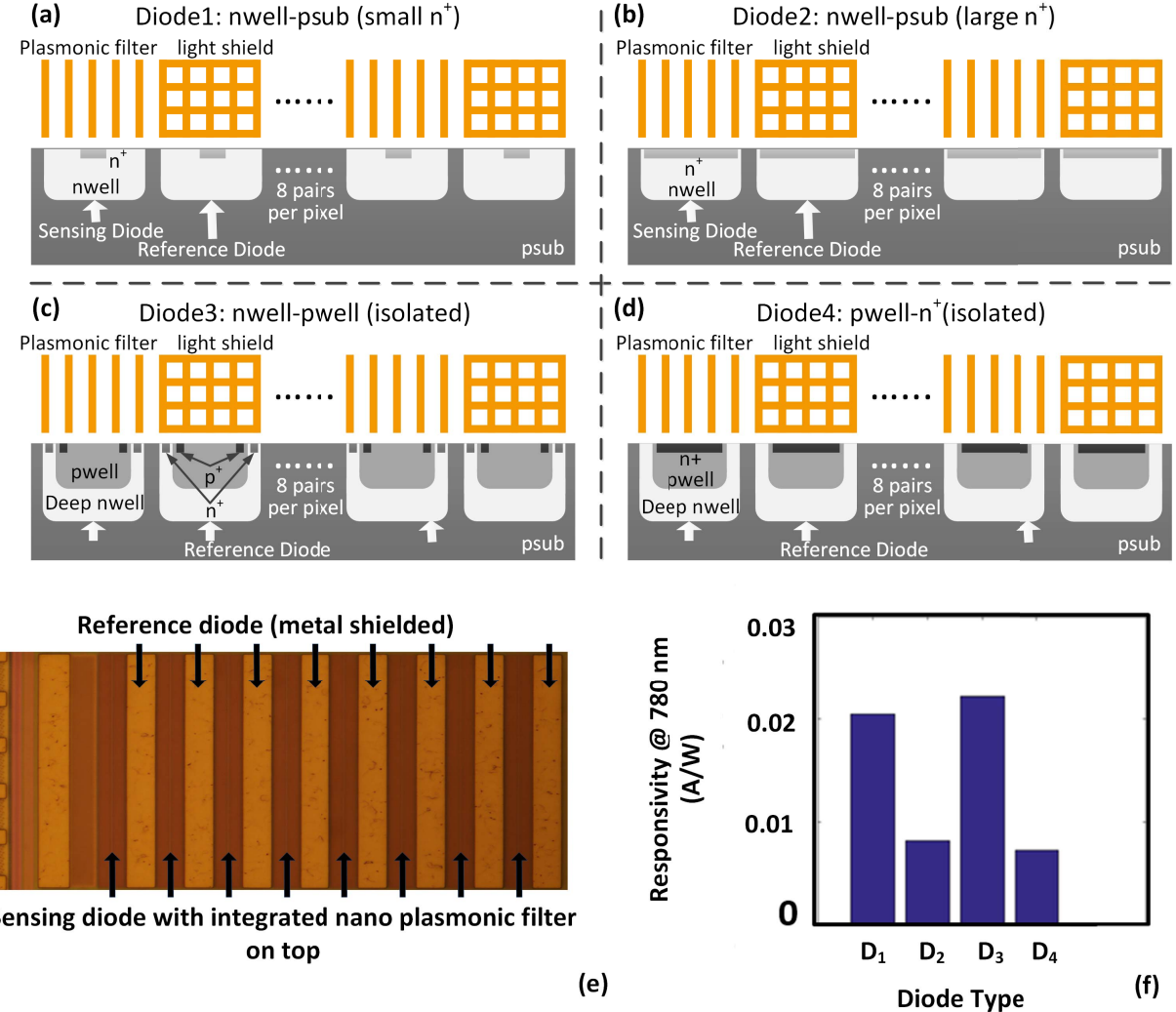


Fig. 14. (a)-(d) Four different photodiodes (n-well/p-sub, n-well/p-sub with larger active region, p-well/n-well, and n+/p-well) realized in the bulk 65-nm CMOS process and (e) inter-digitated layout of the sensing diode. (f) Measured responsivity of the diodes.. This includes the effects of all optical losses, reflections from dielectric interfaces, and quantum efficiency of the diodes.

of the differential signal at two sampling times producing the output $V_{+1} - V_{+2} + V_{-2} - V_{-1}$ devoid of offset. All the capacitors involved in the operation are the same as illustrated in Fig. 16. During the reset period, switches S_3 and S_5 are closed and S_6 is open which results in the charge stored at the OTA's input node (Q_1, Q_2) to be expressed as

$$\begin{aligned} Q_1 &= C[(V_{\text{reset}} - V_{+1}) + (V_{\text{reset}} - V_{\text{ref}})] \\ Q_2 &= C[(V_{\text{reset}} - V_{-1}) + (V_{\text{reset}} - V_{\text{ref}})]. \end{aligned} \quad (4)$$

At time t_2 , the offset is sampled with S_6 closed and S_3 and S_5 opened. Charges Q_1 and Q_2 remain conserved as

$$\begin{aligned} Q_1 &= C[(V_{\text{in}+} - V_{+2}) + (V_{\text{in}+} - V_{\text{out}-})] \\ Q_2 &= C[(V_{\text{in}-} - V_{-2}) + (V_{\text{in}-} - V_{\text{out}+})]. \end{aligned} \quad (5)$$

As shown in Fig. 16, since $(V_{\text{out}+} - V_{\text{out}-}) = A(V_{\text{in}+} - V_{\text{in}-})$, we obtain

$$\begin{aligned} (V_{\text{out}+} - V_{\text{out}-}) &= \left(\frac{A}{A+2} \right) (V_{+1} - V_{+2} + V_{-2} - V_{-1}) \\ &\approx V_{+1} - V_{+2} + V_{-2} - V_{-1}. \end{aligned} \quad (6)$$

Fig. 16 also shows a Monte Carlo simulation of suppression to offset voltages caused by the process variations and mismatch of the differential circuits.

E. Analysis of Circuit Noise Contributions

Stochastic processes in the system contributed by circuit noise, photon shot noise, laser excitation noise, external read-out noise, and biological noise can limit achievable LOD. The total circuit noise processed by CDS primarily consists of thermal noise and shot noise of the related circuit components, while 1/f noise is largely suppressed. In the following, we analyze the effect of the circuit noise processes and analyze the achievable LOD when limited by the noise processes.

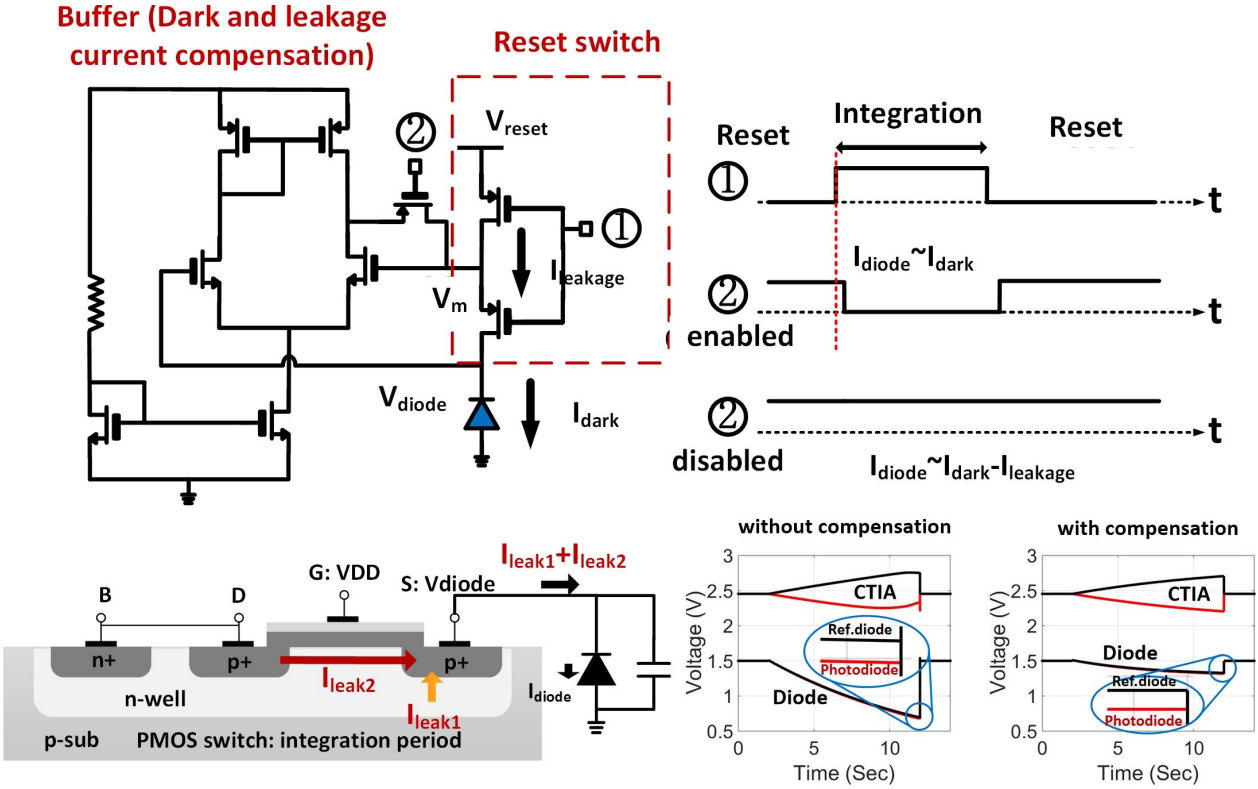


Fig. 15. Leakage current through the PMOS switch can be suppressed by activating the feedback circuitry. Controlling the switch voltage, leakage current can also be exploited to partially suppress the effect of dark current and the reverse-bias current of the photodiode.

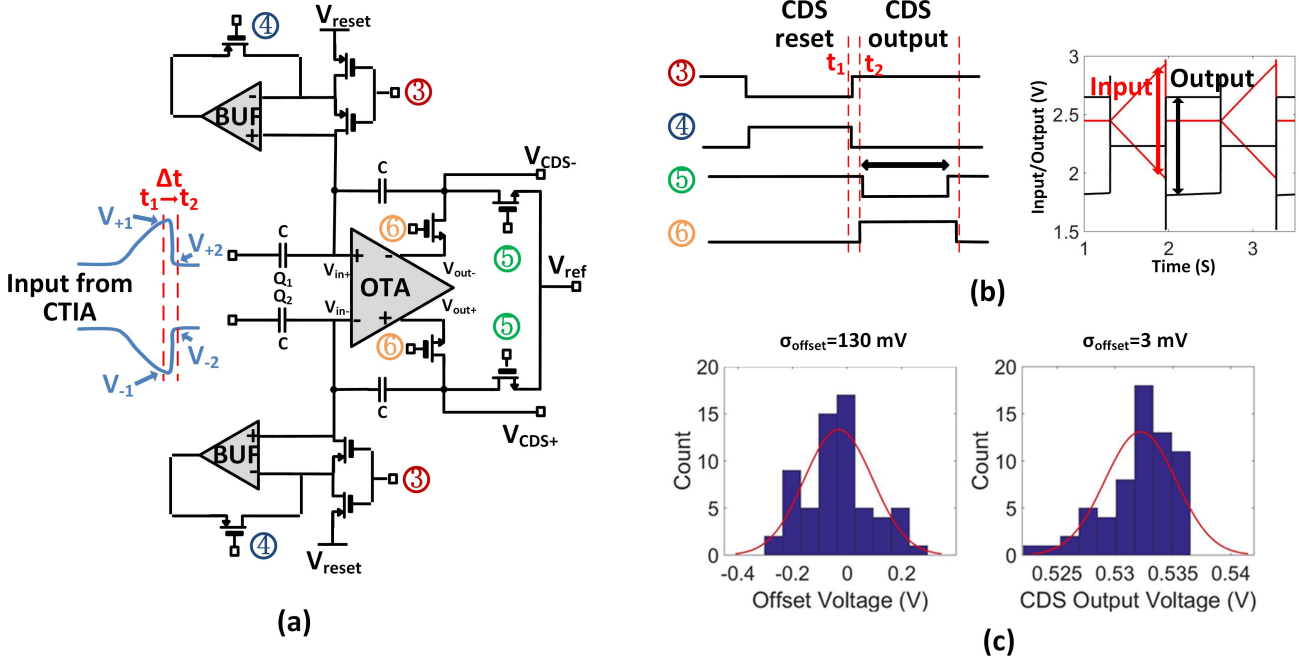


Fig. 16. (a) Correlated double-sampling architecture. (b) Timings of the control signals and measured output voltage of the TIA and the CDS. (c) Reduction of the offset voltage without and with the CDS shown by Monte Carlo simulations.

1) Photon Shot Noise: The photon shot noise is one of the dominant noise sources, as expected. When P_f , P_l , β , and R_f denote the fluorescence emission, the excitation light power, filtering ratio, and responsivity, respectively, the output voltage

noise due to the photon shot noise can be represented as

$$\overline{V_{n,op,ph}^2} = \frac{\left(P_f + \frac{P_l}{\beta} \right) R_f T e}{C_{fb}^2} \quad (7)$$

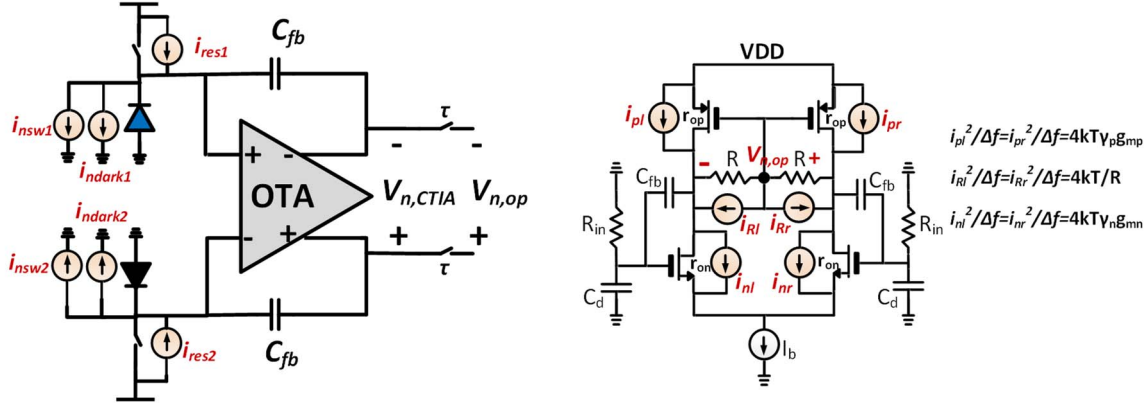


Fig. 17. Noise processes in the architecture.

where T denotes the integration time and e is the electron charge. As shown in Section VI, the signal-to-noise ratio (SNR) improves with T which is ultimately bounded by the allowable voltage swing (V_{sw}) as

$$T \leq T_{\max} = \frac{V_{\text{sw}}C_{\text{fb}}}{(P_f + \frac{P_l}{\beta})R_f}. \quad (8)$$

This sets output noise under full swing due to photon shot noise as $\sqrt{V_{n,\text{ph},\text{op}}^2} = ((V_{\text{sw}}e)/C_{\text{fb}}) \approx 0.84 \text{ mV}$ for $V_{\text{sw}} \approx 1 \text{ V}$. For P_f , $(P_l/\beta) \sim 10-100 \text{ pW}$, expected $T \sim 100 \text{ ms-1 s}$. The shot noise power increases proportionately with supply voltage and integration time, but SNR also improves due to a quadratic increase of signal power with these parameters. This sets a tradeoff between supply voltage, power dissipation, and achievable sensitivity.

2) *Reset Switch Noise:* The circuit model with the various noise components is shown in Fig. 17. R_{in} represents the resistance of the reset switch which leads to a differential noise at the CTIA output as

$$\overline{V_{n,\text{sw},\text{op}}^2}(\text{res}) = \frac{2KTA^2}{C_d + (1 + A)C_{\text{fb}}} \approx \frac{2KTA}{C_{\text{fb}}}. \quad (9)$$

This results in $(\overline{V_{n,\text{sw},\text{op}}^2})^{1/2}(\text{res}) \approx 1.2 \text{ mV}$. During the integration period, when the switch is OFF, the main noise contributor at the CTIA input is the leakage currents of the switch transistors ($i_{\text{nsw}1}, i_{\text{nsw}2},$) and the diode dark currents ($i_{\text{ndark}1}, i_{\text{ndark}2}$). The voltage noise power sampled at intervals of the integration time (τ) after resetting is then the mean square of the time series $V_{n,\text{sw},\text{op}}(t)(\text{int}) = V_{n,\text{CTIA}}(t) - V_{n,\text{CTIA}}(t - \tau)$. This allows us to evaluate the power spectral density and the power of the noise contributed by these sources during the integration period which is dependent on the integration time (τ) as $(\overline{V_{n,\text{sw},\text{op}}^2}(\text{int}))/\Delta f = 4q(I_{\text{sw}} + I_{\text{dark}})((|1 - e^{-j\omega\tau}|^2)/(\omega^2 C_{\text{fb}}^2))$ which gives the total noise voltage as $\overline{V_{n,\text{sw},\text{op}}^2}(\text{int}) = \int_0^\infty ((\overline{V_{n,\text{sw},\text{op}}^2})/\Delta f) df = ((2\tau q(I_{\text{sw}} + I_{\text{dark}}))/(C_{\text{fb}}^2))$. Since $I_{\text{sw}}, I_{\text{dark}} \sim 10-100 \text{ fA}$, their shot noise can be neglected for typical $\tau \sim 100 \text{ ms-1 s}$.

3) *CTIA Noise:* The contributing noise currents of the CTIA are shown in Fig. 17. During the integration period, the switch transistor is OFF and the noise voltage can be approximated

as $\overline{V_{n,\text{CTIA},\text{op}}^2}(\text{int}) = (4KT/\pi C_d)((C_d + C_{\text{fb}})/C_{\text{fb}})^2(g_{mn}r_{\text{on}} + g_{mp}r_{\text{op}})$. As expected the noise increases proportionality with the trans-conductance, while the signal increases quadratically. This leads to an expected tradeoff between SNR and power dissipation. The TIA is designed to consume 6 mW of power, which results in $(\overline{V_{n,\text{CTIA},\text{op}}^2})^{1/2}(\text{int}) \approx 0.649 \text{ mV}$ during the integration period, while during reset phase $(\overline{V_{n,\text{CTIA},\text{op}}^2})^{1/2}(\text{res}) \approx 0.653 \text{ mV}$. Taking all these sources into account, the total rms. noise during fluorescence detection can be estimated as $(\overline{V_{n,\text{op}}^2})^{1/2} \approx 1.7 \text{ mV}$.

It should also be noted that the effects of circuit noise are dependent on the sampling scheme. By directly sampling, the CTIA output with a high-resolution ADC, and applying a linear regression to determine the slope of the output and integration time, one can minimize the effective noise power and improve SNR. As shown later in the measurement results in Fig. 25, modeling the output of the CTIA as $V_i = \alpha + \beta t_i + \epsilon_i$, where $t_i = it_s$ are the sampling times and ϵ_i is the sampled white noise process of variance σ_ϵ^2 ; the regression slope obtained from least-squares estimation satisfies $\beta_{\text{regression}} = \beta + ((\sum t_i \epsilon_i - (1/N) \sum t_i \sum \epsilon_i)/(\sum t_i^2 - (1/N)(\sum t_i)^2))$. This results in the standard deviation of $\beta_{\text{regression}}$ as $\sigma_\beta = (12/(N(N-1)(N+1)))^{1/2} \sigma_\epsilon$. The output noise voltage is then given by

$$\sqrt{\overline{V_{n,\text{op}}^2}} = (t_N - t_1)\sigma_\beta \approx \sqrt{\frac{12}{N}}\sigma_\epsilon. \quad (10)$$

This noise suppression also holds for the quantization noise $((\overline{V_{n,\text{ADC}}^2})^{1/2})$ at the data acquisition interface. Therefore, this illustrates that with linear regression, the total noise $(\overline{V_{n,\text{op}}^2} + \overline{V_{n,\text{ADC}}^2})^{1/2}$ can be reduced by a factor of $(12/N)^{1/2}$ using a large number of samples, as long as the noise samples are uncorrelated. However, in practice, there are residual correlated noise components that limit the achievable noise reduction, as will be seen later in measurement results. These arise due to the 1/f noise as well as due to the white noise components when processed through frequency-dependent transfer functions of the various circuit elements, as captured in the analysis.

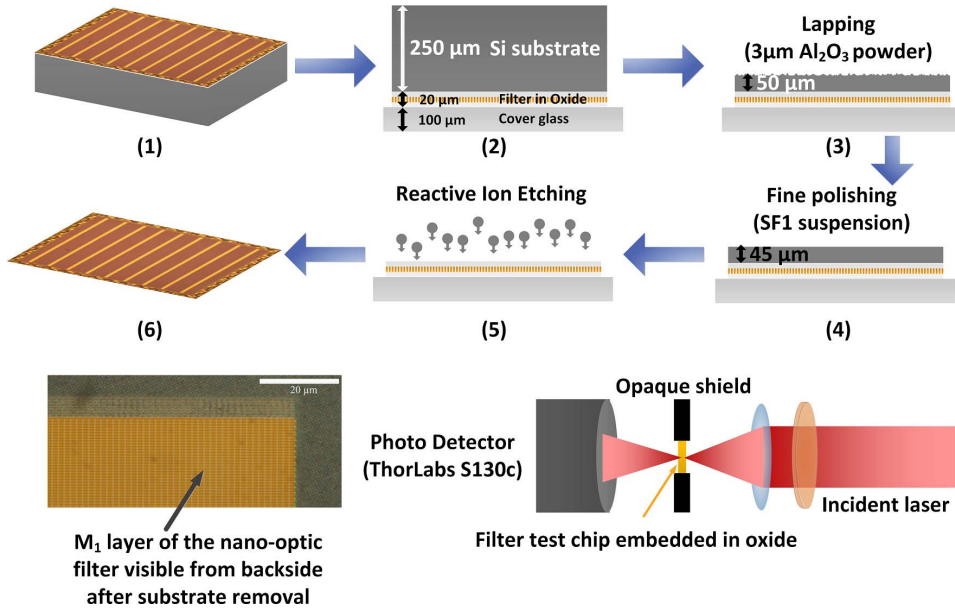


Fig. 18. Precise removal of the silicon substrate to separate the nano-optic filter embedded in the dielectric and free-space measurement of the spectral responsivity.

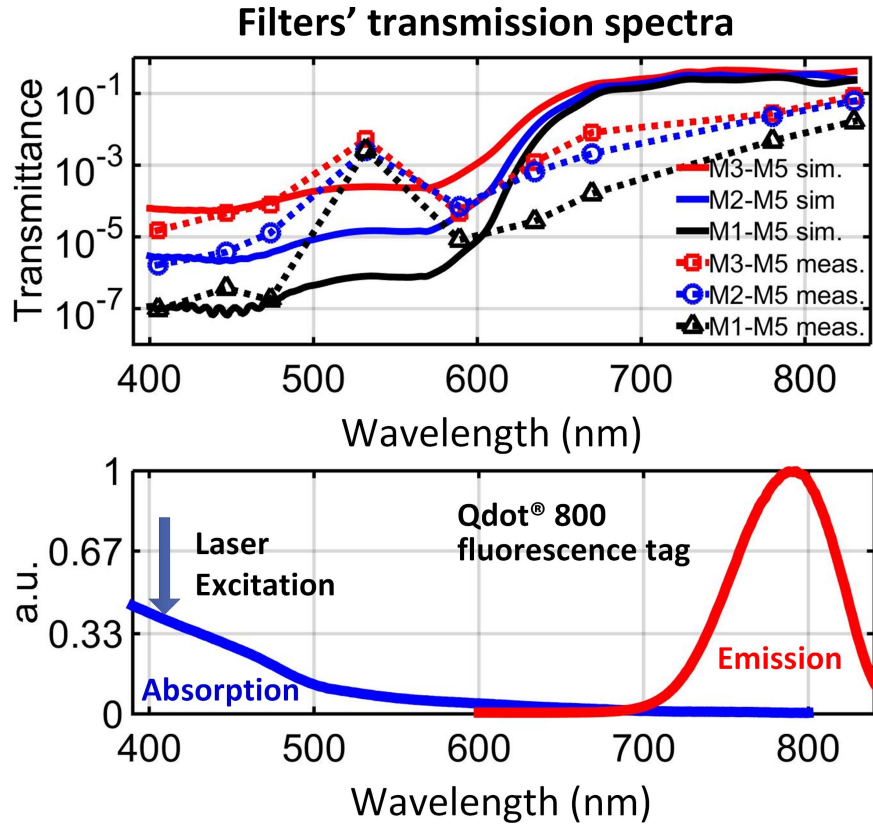


Fig. 19. Measured and simulated transmission spectra of the integrated filters and the emission and excitation spectrum of streptavidin-coated Qdot 800 [47].

VI. MEASUREMENT RESULT

The fluorescence biosensor and test structures such as the nanophotonic filters are implemented in a standard 65-nm LP CMOS process. The process supports ten metal layers of copper with the lowest five having 100-nm minimum lithographic linewidth and 130-nm spacing.

A. Nanoplasmonic Filter Characterization

The integrated filters were measured with two different setups. First, the filter performance was measured directly with the on-chip photodetectors. This was done by measuring the response of the bare photodiode test structures (without the filters) and subsequently measuring the photodiode test

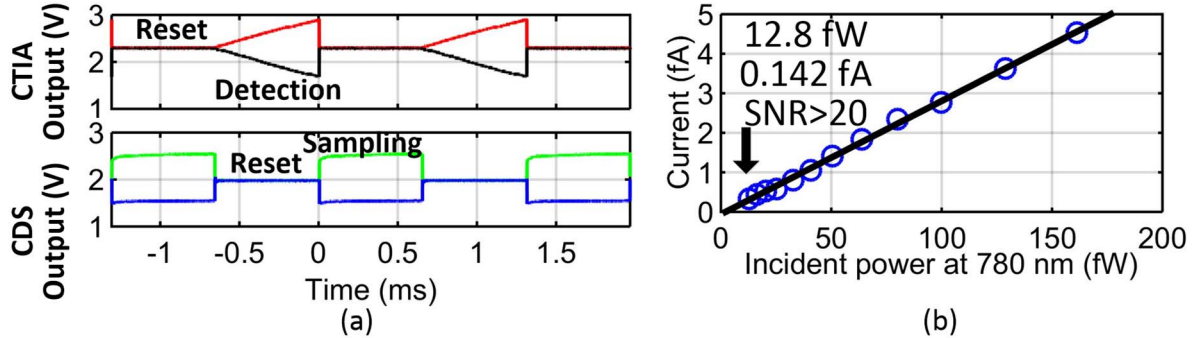


Fig. 20. (a) Measured output waveforms of the CTIA and CDS. (b) Responsivity of the bare photodetector without any filter at the fluorescence wavelength of 780 nm.

structures with the filters. To remove the uncertainty due to the process variations in the two sets of diodes, the optical filters were also measured with a free-space optical setup. This was done by removing the back side of the silicon substrate precisely to isolate the filter test structures embedded in the dielectric. As shown in Fig. 18, in order to ensure a flat and uniform back-side surface, the steps include the following:

- 1) lapping of the substrate to around $50\text{-}\mu\text{m}$ thickness using Al_2O_3 abrasive powder of $3\text{-}\mu\text{m}$ size;
- 2) fine polishing using SF1 (Alkaline colloidal silica) polishing suspension;
- 3) reactive ion etching of the remaining Si layer.

The exposure of the embedded M_1 layer, after removing the substrate, is shown in a micrograph in Fig. 18. To verify the physics of operation of the filter, test structures with varying numbers of metal layers (3, 4, and 5 denoted by $M_3\text{-}M_5$, $M_2\text{-}M_5$, and $M_1\text{-}M_5$) and with varying thicknesses (1, 1.38, and $1.77\text{ }\mu\text{m}$) are fabricated and measured. The measured transmission spectra in Fig. 19 demonstrate rejection ratios to be 35, 43, and 50 dB between the excitation wavelength at 405 nm and emission wavelength near 800 nm. The spectral configuration matches with the fluorescence Qdot of interest, Qdot 800 (Life Technologies [52]) whose excitation and emission spectra are also shown in Fig. 19. The simulated values of the nano-optic filter of pure copper embedded in silicon dioxide are around 37.7, 50.8, and 63.8 dB, respectively. The difference in the measured against simulated rejection ratio is often observed in plasmonic structures, primarily because SPP is a strong surface phenomenon and surface properties can significantly influence the SPP modes. In a CMOS process, this could be attributed to a variety of reasons such as exact composite of the Cu material, the barrier diffusion layer (TaN/Ta, AlOx, or MnOx), seed layers (Al/ALCu) as well as capping barrier dielectrics (SiN/SiC/SiCN), the low-K dielectric material composite, and interference at multiple dielectric interfaces. Inspite of this, a filtering ratio of 50 dB is measured with the CMOS nanoplasmatic filters between the excitation and emission wavelengths for the chosen fluorophore.⁴

⁴The peaking at 540 nm is likely due to a complex interaction of the SPP mode and multiple reflections at the various interfaces of the multiple dielectric stacks in the BEOL.

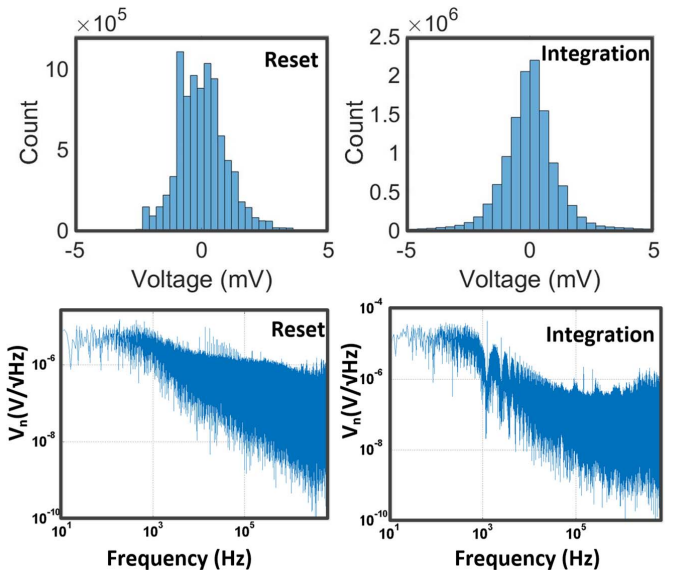


Fig. 21. Measured noise voltage and spectrum of the diode at reset and integration operations under dark.

B. Sensor Circuitry Characterization and Measurement

The output waveforms of the differential CTIA and CDS under normal operation of bare photodiodes (without any integrated filter) are shown in Fig. 20(a). The responsivity of the photodiode at the emission wavelength of 780 nm measured by varying the incident power from a 780-nm laser with continuously variable neutral density optical filters is shown in Fig. 20(b). In calculating sensor responsivity, the entire light power incident on the whole sensor area including the shielded diode is taken into consideration. Multiple measurements at the output with a high-resolution digitizer also enable us to evaluate output SNR. As an example for optical power of 12.8 fW, the photocurrent measures 0.142 fA for a measured $\text{SNR} > 13$ dB with 10-s integration. Under dark condition, the total circuit noise is measured to be $(V_{n,\text{op}}^2)^{1/2} \approx 1.31\text{ mV}$ ($(\overline{V_{n,\text{op}}^2})^{1/2}(\text{res}) \approx 0.94\text{ mV}$, $(\overline{V_{n,\text{op}}^2})^{1/2}(\text{int}) \approx 0.91\text{ mV}$) close to the predicted value of $(\overline{V_{n,\text{op}}^2})^{1/2} \approx 1.51\text{ mV}$. The slightly higher value of the predicted noise is likely due to the overestimation of the intrinsic gains and output resistances of the stages. The measured distribution of the output signal

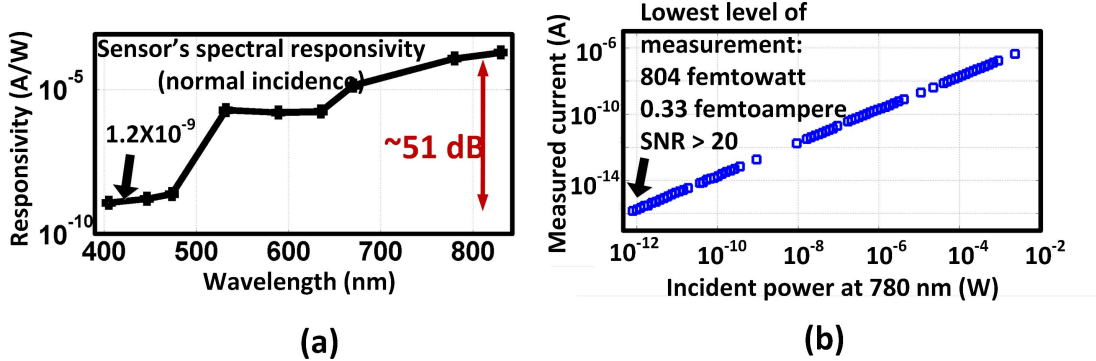


Fig. 22. (a) Measured spectral responsivity of the sensor with the integrated filter. (b) Detection limit and dynamic range of the sensor at the fluorescence wavelength.

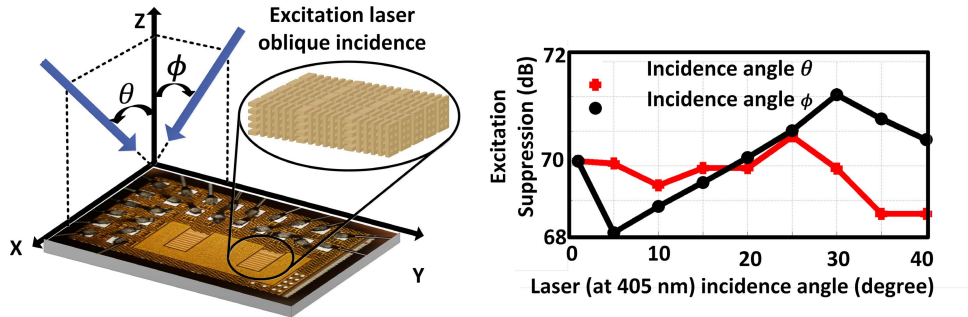


Fig. 23. Measured performance of the filter with variation in angle of incidence of the excitation laser.

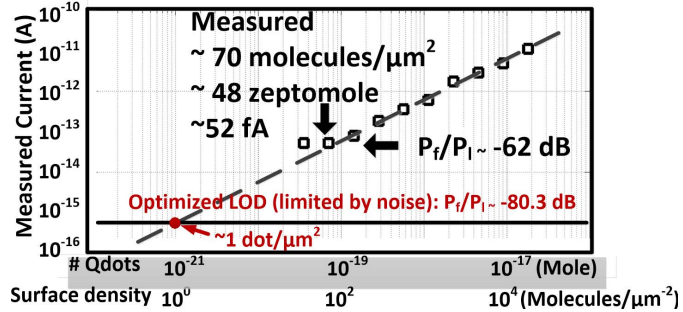


Fig. 24. Measured streptavidin-coated fluorophore detection sensitivity. Optimal LOD for the presented biosensor chip is achieved when the sensitivity is limited by noise when residual scattering is eliminated by optical packaging.

variations through multiple measurements and the captured noise spectra is shown in Fig. 21. The noise measured under excitation with fluorescence signal with full voltage swing is measured to be $(V_{n,\text{op}}^2)^{1/2} \approx 2.2 \text{ mV}$, slightly higher than the predicted value of $(V_{n,\text{op}}^2)^{1/2} \approx 1.71 \text{ mV}$. It can be noted that in spite of the low quantum efficiencies of the diodes in the 65-nm LP process, femto-watt level light detection is achievable owing to longer integration times made possible with dark and leakage current suppression techniques. The measured surface temperature of the chip due to the dc power dissipation is $3.8 \text{ }^\circ\text{C}$ above the room temperature which is acceptable for bio-molecular sensing.

C. Optical and Electronic Performance Characterization

The measured spectral responsivity of the sensor chip with integrated nanophotonic filter, measured from the CTIA output, is shown in Fig. 22, demonstrating a filtering ratio

of 51 dB . This includes the spectral dependence of the photodiode and dielectric interfaces. Due to higher than expected transmission loss, detection limit of the sensor with the integrated filter is measured to be 804 fW at 780 nm [Fig. 22(b)]. The figure also shows that the response is highly linear and the measured dynamic range exceeds 94 dB. The filter was also tested for its rejection properties at different angles of incidences. As shown in Fig. 23(a) and (b), the sensor can reject excitation light up to 70 dB as the angle of incident varies from 0° to 40° and similar rejection for higher angles of incidence is expected from its physics of operation. This eliminates the need for external collimators and enables light coupled form directly from the fluorescence dipoles on the chip surface to be detected, while rejecting the background and the scattered incident light. Furthermore, the non-resonant nature of the filters allows the use of low-cost sources such as LEDs at 405 nm useful for miniaturized systems.

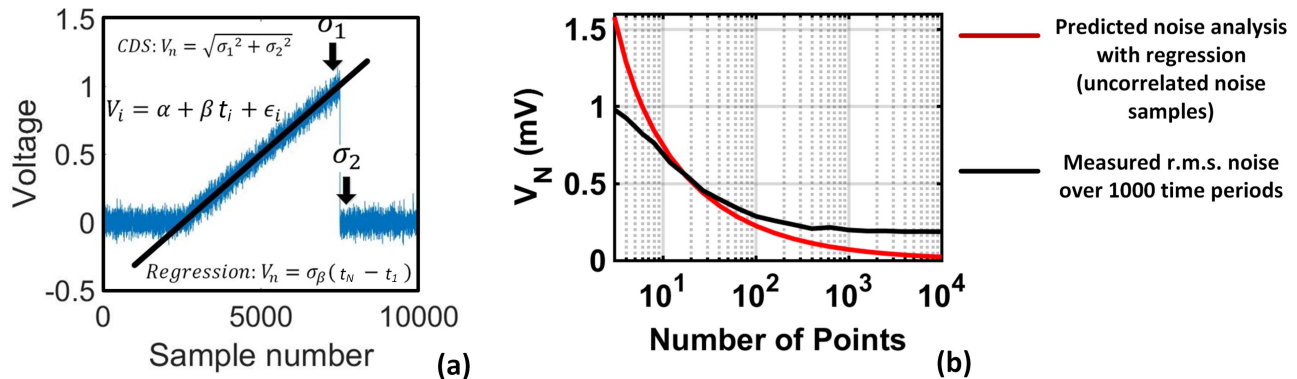


Fig. 25. (a) Effective noise power reduction with regression based estimation at the CTIA output measured with a high resolution ADC. (b) Reduction of noise rms. voltage with increase in number of samples for regression with one time period. Since the predicted noise analysis assumed uncorrelated noise samples, the measured reduced noise voltage exceeds the predicted value due to correlated noise components when very large number of densely placed samples is taken.

TABLE I
CHIP PERFORMANCE TABLE

Technology	65 nm bulk CMOS	Bare Diode Sensitivity	12.8 fW
DC Power	66 mW (Dual sensors) (TIA, CDS≈ 6.0 mW, Buffer=2.6 mW)	Diode with Filter Sensitivity	804 fW
Sensor size	0.4x0.8 mm²	Optical Filter	Integrated nano-plasmonic filter
Photodiode Size	91.4 X 123 μm²	Excitation Collimation	Not required
Differential Dark Current	15.5 fA	Fluorescence Tag Used	Qdot 800
Quantum Efficiency	7%	Detection Limit (Density)	70 molecules/μm²
Excitation Laser	405 nm diode laser	Detection Limit (Total)	48 zepto moles

D. Biosensor Measurements

The sensitivity of a biosensor is characterized by its surface sensitivity, i.e., the minimum number and surface density of bio-molecules/labels it can measure with a given SNR. The translation of volume sensitivity (molar concentration) to surface density in a bio-assay is governed by many factors including geometry of the fluid handling, diffusion mechanisms, surface functionalization, capture efficiency, and the bio-chemistry protocol. The surface density of detectable fluorophores is characterized with a 0.5 μL drop of streptavidin-coated Qdot 800 solution of varying concentration on the sensor surface.⁵ As shown in Fig. 24, a nearly linear response was obtained for surface densities from 1820 dots/μm² down to 70 dots/μm² when measured under dark ambient conditions. This level of sensitivity corresponds to only 48 zeptomoles of

fluorophores. The surface density of the Qdots was verified with a calibrated curve of volume concentrations and surface concentrations under a fluorescence microscope. Currently, without any optical shielding or packaging (Fig. 1), the LOD is limited by external stray light scattering (from wire bonds, pads, etc.) which couple to the chip bypassing the filters, limiting integration time, and achievable sensitivity. This can be improved with opaque epoxy packaging and improved on-chip shielding. The achievable LOD for the chip, then approaches 1 dot/μm² with the fluorescence signal being 80 dB lower than the excitation light. Table I presents the summary of chip performance. As shown in Section V-E, the output noise can be suppressed by directly sampling the output and applying regression on the sampled data over a time period [Fig. 25(a)]. The measured reduction of rms. noise voltage with number of sampled data points (N) used for regression is shown in Fig. 25(b). As can be seen, the measured noise reduces with N , but exceeds the predicted analysis in (10) for very large values of N . This is primarily because the noise analysis in (10) assumes uncorrelated noise samples. The

⁵For a bio-assay, the surface is typically functionalized with capture probes which can be done with μm accuracy over thousands of sensors. This technology is well-matured and can be done at a low-cost and currently carried out in commercially available gene chips as well. This allows very accurate positioning of the quantum dots on the chip surface.

TABLE II

ACHIEVABLE FLUORESCENCE LIMIT OF DETECTION (FLOD) FOR THE PRESENTED BIOSENSOR CHIP WHEN THE SENSITIVITY IS LIMITED BY NOISE WITH OPTICAL SHIELDING THAT CAN ELIMINATE THE RESIDUAL SCATTERED LIGHT. THE NOISE AND SYSTEM PARAMETERS ENLISTED IN THE TABLE ARE DEFINED IN THE APPENDIX

Parameters	Values	Parameters	Practical Values
β	51 dB (measured)	V_{SW}	1 V (measured)
η_{ex}	7.36×10^{-4} (measured)	C_{fb}	226 fF
$\sqrt{V_{Ncir}^2 + V_{Nadc}^2}$	0.19 mV (measured, regression based)	η_{bio}	~20% (estimated)
Fluorescence Limit of Detection (FLOD)	$\frac{P_f}{P_l} = -80.3 \text{ dB}$		

TABLE III
COMPARISON TABLE WITH THE STATE OF THE ART

Technology	This Work	[16]	[17]	[19]	[65]	[66]	[67]
	65 nm	N.A.	0.18 μm	0.35 μm	0.18 μm	0.35 μm	0.11 μm
Optical Filter	Integrated nano-plasmonic filter	External thin film interference filter ZnS/Na ₃ AlF ₆	Time gated electronic filtering	External assembled thin film interference filter	External spin coated absorption filter (98 μm)	External assembled thin film interference filter (100 μm thick)	Time gated electronic filtering
Excitation Collimation	Not required	Fiber optical faceplate	Not required	Not required	Not required	External collimator used with LED excitation	Not required
Excitation Laser	405 nm diode laser	532 nm DPSS	406 nm picosecond pulsed laser	532 nm	340 nm	450 nm	472 nm picosecond pulsed laser
DC power	66 mW (Dual Sensors)	N.A.	250 mW*	26.2 mW*	N.A.	N.A.	540mW*
Laser Power	4 mW	N.A.	150 mW peak power	10 mW	N.A.	10 mW	47 mW peak power
Fluorescence Tag Used	Qdot 800	Cy3	Qdot 655	Cy3	N.A. designed for > 450 nm tag	Qdot 520, 620	DAPI and Qdot
Photodiode Area	91.4 X 123 μm^2	50 X 50 μm^2	50 X 50 μm^2	15.4 X 15.4 μm^2	7 X 7 μm^2	50 X 50 μm^2	11.2 X 5.6 μm^2
Detection Limit	70 molecules/ μm^2 or 48 zepto moles (measured) Achievable LOD with better packaging/external optical shielding: 1 molecules/ μm^2 (0.70 zepto moles)	20 molecules/ μm^2	3.2×10^5 molecules/ μm^2	5000 molecules/ μm^2	Not reported	~2.1 pmoles of Qdot labeled DNA ~ 10^5 molecules/ μm^2 (estimated from sensor area)	Not reported

reduced noise voltage is ultimately limited by the correlated noise components when very large number of densely placed samples is taken. As explained in Section V-E, the residual correlated noise arises out of 1/f noise and white noise processed through the frequency-dependent transfer functions of the various circuit elements. Applying this method, the total rms. noise is measured to be 0.19 mV for $N = 1600$, which further improves the achievable LOD, as shown in Table II.

While the biosensor LOD can be defined as the minimum surface density of fluorescence labels for a given SNR, this metric is dependent on the particular fluorescence tag used. To dissociate the quality of the fluorescence sensor from the

tag, we define fluorescence LOD (FLOD) as the minimal fluorescence-to-excitation signal (P_f/P_l) for a SNR of 1. The dependence of this metric on the various system and noise parameters is derived in the Appendix. With measured laser stability of $\eta_{ex} \approx 7.36 \times 10^{-4}$, typical biological uncertainty (η_{bio}) of 20%, the achievable FLOD (SNR = 1) for the presented biosensor with the on-chip filter can reach toward $P_f/P_l = -80$ dB corresponding to sensor LOD of 1 molecule/ μm^2 (Fig. 24). In the limit, FLOD is limited by laser fluctuations (η_{ex}) when P_f/P_l approaches -82 dB even if all the noise sources are eliminated. Therefore, much larger enhancement of performance can be achieved by eliminating

$$\text{SNR} = \frac{\frac{P_f R_f T}{e}}{\sqrt{\underbrace{\left(\frac{V_{\text{Ncir}} C_{\text{fb}}}{e}\right)^2}_{\text{Circuit noise}} + \underbrace{\left(\frac{V_{\text{Nadc}} C_{\text{fb}}}{e}\right)^2}_{\text{Quant. noise}} + \underbrace{\left(\frac{(P_f + \frac{P_l}{\beta}) R_f T}{e}\right)}_{\text{Shot noise}} + \underbrace{\left(\frac{(2I_d)T}{e}\right)}_{\text{Dark current shot noise}} + \underbrace{\left[\frac{\eta_{\text{ex}} \left(P_f + \frac{P_l}{\beta}\right) R_f T}{e}\right]^2}_{\text{Laser fluctuation noise}} + \underbrace{\left(\frac{\eta_{\text{bio}} P_f R_f T}{e}\right)^2}_{\text{Biological noise}}}} \quad (11)$$

residual background scattering with improved optical packaging and on-chip optical shielding, effectively increasing β . Table III shows the chip performance with prior work showing the state-of-the-art sensitivity ($70 \text{ mol}/\mu\text{m}^2$) with no post-processing, collimators, or external synchronization requirements.

VII. CONCLUSION

In conclusion, we present, for the first time, copper-based nanoplasmmonic components in standard CMOS that can controllably manipulate optical fields enabling complex multi-functional optical structures in CMOS. This is achieved by exploiting interaction of light with sub-wavelength lithographic metal features in modern CMOS processes. In particular, we present a fully integrated CMOS-based fluorescence biosensor with nano-waveguide array-based filter achieving more than 50 dB of measured rejection and capable of detection of 48 zeptomoles of Qdot-based fluorophores on the surface. The ability to integrate these optical components also creates the opportunity to enable massively parallelized sensing sites on a single chip, enabling a great variety of applications, from *in vitro* to *in vivo*.

APPENDIX

In this appendix, we analyze the dependence of the sensor's FLOD on the various system parameters such as the filter rejection ratio, filter losses, quantum efficiency, noise processes, and propose methods to improve the achievable FLOD. Consider a fluorescence sensing setup with the following parameters: fluorescence light power (P_f), the filtering ratio β , photodiode responsivity at the fluorescence wavelength (R_f), excitation wavelength (R_f/β), integration time (T), photo-sensing circuits noise (V_{Ncir}), and external ADC read-out noise (V_{Nadc}), average dark current of the photodiode (I_d), normalized standard deviations of laser excitation power (η_{ex}), and biological signal (η_{bio}).⁶ Therefore, the SNR for the biosensor represented in terms of electrons generated at the photodiode can be expressed as (11), as shown at the top of this page.

⁶ η_{bio} represents percentage fluctuation subject to fluidic handling, chemical reaction, molecular diffusion and uncertainty in the binding events. As an example, if N_{QD} is the number of QDots captured in an experiment and $\eta_{\text{bio}} = ((\sigma(N_{\text{QD}}))/(\mu(N_{\text{QD}})))$, then the signal measured from the fluorescence expressed in number of electrons $N_{\text{sig}} \propto N_{\text{QD}}$, which results in $((\sigma(N_{\text{sig}}))/(\mu(N_{\text{sig}}))) = ((\sigma(N_{\text{QD}}))/(\mu(N_{\text{QD}}))) = \eta_{\text{bio}}$. This gives us $\sigma(N_{\text{sig}}) = (\eta_{\text{bio}} P_f R_f T)/e$ as expressed in (11).

As can be seen, SNR increases monotonically with integration time T and the measured SNR with variation in integration time shows this expected square-root dependence (Fig. 24). Since $T \leq T_{\max} = ((V_{\text{sw}} C_{\text{fb}})/((P_f + (P_l/\beta)) R_f))$. Therefore, FLOD or the minimal fluorescence-to-excitation signal (P_f/P_l) for $\text{SNR} = 1$ can be shown to satisfy

$$\begin{aligned} \frac{P_f}{P_l}|_{\text{SNR}=1} &= \frac{1}{\beta} \frac{1}{\sqrt{\frac{1 - \eta_{\text{bio}}^2}{\eta_{\text{ex}}^2 + \frac{V_{\text{Ncir}}^2 + V_{\text{Nadc}}^2}{V_{\text{sw}}^2} + \frac{e}{V_{\text{sw}} C_{\text{fb}}}} - 1}} \\ &\approx \frac{1}{\beta} \sqrt{\frac{\eta_{\text{ex}}^2 + \frac{V_{\text{Ncir}}^2 + V_{\text{Nadc}}^2}{V_{\text{sw}}^2} + \frac{e}{V_{\text{sw}} C_{\text{fb}}}}{1 - \eta_{\text{bio}}^2}}. \end{aligned} \quad (12)$$

As can be seen, the sensitivity has a direct tradeoff with power through the noise components V_{Ncir} and V_{Nadc} as well as the supply voltage V_{sw} . The dependence of the circuit noise on dc power consumption is explained in Section V-E. Additionally, it can be seen that the minimal detectable signal is inversely proportional to the filter's rejection ratio, while the absolute responsivity or quantum efficiency is not significant when the sensitivity is limited by background.

ACKNOWLEDGMENT

The authors would like to thank National Science Foundation and Qualcomm Innovation Fellowship for support, IBM and Dr. W. Chappell, DARPA, for chip fabrication and support, and all members of the Integrated Microsystems Research Lab for their technical discussions.

REFERENCES

- [1] V. Gubala, "Point of care diagnostics: Status and future," *Anal. Chem.*, vol. 84, no. 2, pp. 487–515, Jan. 2012.
- [2] J. Rosenstein, M. Wanunu, C. A. Merchant, M. Drndic, and K. L. Shepard, "Integrated nanopore sensing platform with sub-microsecond temporal resolution," *Nature Methods*, vol. 9, no. 5, pp. 487–492, May 2012.
- [3] B. Jang and A. Hassibi, "Biosensor systems in standard CMOS processes: Fact or fiction?" *IEEE Trans. Ind. Electron.*, vol. 56, no. 4, pp. 979–985, Apr. 2009.
- [4] H. Lee, E. Sun, D. Ham, and R. Weissleder, "Chip-NMR biosensor for detection and molecular analysis of cells," *Nature Med.*, vol. 14, no. 8, pp. 869–874, Jul. 2008.
- [5] H. M. Jafari, K. Abdelhalim, L. Soleymani, E. H. Sargent, S. O. Kelley, and R. Genov, "Nanostructured CMOS wireless ultra-wideband label-free PCR-free DNA analysis SoC," *IEEE J. Solid-State Circuits*, vol. 49, no. 5, pp. 1223–1241, May 2014.
- [6] P. M. Levine, P. Gong, R. Levicky, and K. L. Shepard, "Active CMOS sensor array for electrochemical biomolecular detection," *IEEE J. Solid-State Circuits*, vol. 43, no. 8, pp. 1859–1871, Aug. 2008.

- [7] A. Manickam, A. Chevalier, M. McDermott, A. D. Ellington, and A. Hassibi, "A CMOS electrochemical impedance spectroscopy (EIS) biosensor array," *IEEE Trans. Biomed. Circuits Syst.*, vol. 4, no. 6, pp. 379–390, Dec. 2010.
- [8] Y. T. Liao, H. Yao, A. Lingley, B. Parviz, and B. P. Otis, "A 3- μ W CMOS glucose sensor for wireless contact-lens tear glucose monitoring," *IEEE J. Solid-State Circuits*, vol. 47, no. 1, pp. 335–344, Jan. 2012.
- [9] H. Wang, Y. Chen, A. Hassibi, and A. Hajimiri, "A frequency-shift CMOS magnetic biosensor array with single-bead sensitivity and no external magnet," in *IEEE Int. Solid-State Circuits Conf. Dig. Tech. Papers*, Feb. 2009, pp. 438–439.
- [10] S. Gambini *et al.*, "A CMOS 10kpixel baseline-free magnetic bead detector with column-parallel readout for miniaturized immunoassays," in *IEEE Int. Solid-State Circuits Conf. Dig. Tech. Papers*, Feb. 2012, pp. 126–127.
- [11] P. Liu, K. Skucha, M. Megens, and B. Boser, "A CMOS hall-effect sensor for the characterization and detection of magnetic nanoparticles for biomedical applications," *IEEE Trans. Magn.*, vol. 47, no. 10, pp. 3449–3451, Oct. 2011.
- [12] D. A. Hall, R. S. Gaster, S. J. Osterfeld, K. Makinwa, S. X. Wang, and B. Murmann, "A 256 channel magnetoresistive biosensor microarray for quantitative proteomics," *IEEE J. Solid-State Circuits*, vol. 48, no. 5, pp. 1290–1301, May 2013.
- [13] S.-J. Han, H. Yu, B. Murmann, and N. Pourmand, "A high-density magnetoresistive biosensor array with drift-compensation mechanism," in *IEEE Int. Solid-State Circuits Conf. Dig. Tech. Papers*, Feb. 2007, pp. 168–169.
- [14] L. R. Joseph, Ed., *Principles of Fluorescence Spectroscopy*. New York, NY, USA: Springer, 2013.
- [15] B. Jang, P. Cao, A. Chevalier, A. Ellington, and A. Hassibi, "A CMOS fluorescent-based biosensor microarray," in *IEEE Int. Solid-State Circuits Conf. Dig. Tech. Papers*, Feb. 2009, pp. 436–437.
- [16] T. C. D. Huang, S. Sorgenfrei, P. Gong, R. Levicky, and K. L. Shepard, "A 0.18- μ m CMOS array sensor for integrated time-resolved fluorescence detection," *IEEE J. Solid-State Circuits*, vol. 44, no. 5, pp. 1644–1654, May 2009.
- [17] H. J. Yoon, S. Itoh, and S. Kawahito, "A CMOS image sensor with in-pixel two-stage charge transfer for fluorescence lifetime imaging," *IEEE Trans. Electron Devices*, vol. 56, no. 2, pp. 214–221, Feb. 2009.
- [18] R. R. Singh, D. Ho, A. Nilchi, G. Gulak, P. Yau, and R. Genov, "A CMOS/thin-film fluorescence contact imaging microsystem for DNA analysis," *IEEE Trans. Circuits Syst. I, Reg. Papers*, vol. 57, no. 5, pp. 1029–1038, May 2010.
- [19] D. Tyndall, B. Rae, D. Li, J. Richardson, J. Arlt, and R. Henderson, "A 100 Mphoton/s time-resolved mini-silicon photomultiplier with on-chip fluorescence lifetime estimation in 0.13 μ m CMOS imaging technology," in *IEEE Int. Solid-State Circuits Conf. Dig. Tech. Papers*, Feb. 2012, pp. 122–124.
- [20] D. Ho, M. O. Noor, U. J. Krull, G. Gulak, and R. Genov, "CMOS tunable-wavelength multi-color photogate sensor," *IEEE Trans. Biomed. Circuits Syst.*, vol. 7, no. 6, pp. 805–819, Dec. 2013.
- [21] K. K. Ghosh *et al.*, "Miniaturized integration of a fluorescence microscope," *Nature Methods*, vol. 8, no. 10, pp. 871–878, Sep. 2011.
- [22] G. Patounakis, K. L. Shepard, and R. Levicky, "Active CMOS array sensor for time-resolved fluorescence detection," *IEEE J. Solid-State Circuits*, vol. 41, no. 11, pp. 2521–2530, Nov. 2006.
- [23] D. Stoppa, D. Mosconi, L. Pancheri, and L. Gonzo, "Single-photon avalanche diode CMOS sensor for time-resolved fluorescence measurements," *IEEE Sensors J.*, vol. 9, no. 9, pp. 1084–1090, Sep. 2009.
- [24] D. H. Ta-Chien, *et al.*, "Gene expression analysis with an integrated CMOS microarray by time-resolved fluorescence detection," *Biosensors Bioelectron.*, vol. 26, pp. 2660–2665, Apr. 2011.
- [25] A. Wang and A. Molnar, "A light-field image sensor in 180 nm CMOS," *IEEE J. Solid-State Circuits*, vol. 47, no. 1, pp. 257–271, Jan. 2012.
- [26] C. Lee, B. Johnson, and A. Molnar, "An on-chip 72 \times 60 angle-sensitive single photon image sensor array for lens-less time-resolved 3-D fluorescence lifetime imaging," in *Symp. VLSI Circuits Dig. Tech. Papers*, 2014.
- [27] H. Norian, I. Kymmissis, and K. L. Shepard, "Integrated CMOS quantitative polymerase chain reaction lab-on-chip," in *Symp. VLSI Circuits Dig. Tech. Papers*, Sep. 2013, pp. C220–C221.
- [28] R. M. Field and K. L. Shepard, "A 100-fps fluorescence lifetime imager in standard 0.13- μ m CMOS," in *Symp. VLSI Circuits Dig. Tech. Papers*, 2013, pp. C10–C11.
- [29] L. Hong, S. McManus, H. Yang, and K. Sengupta, "A fully integrated CMOS fluorescence biosensor with on-chip nanophotonic filter," in *Symp. VLSI Circuits Dig. Tech. Papers*, 2015, pp. C206–C207.
- [30] (2014). *Advancing Moore's Law*. [Online]. Available: http://download.intel.com/newsroom/kits/14nm/pdfs/Intel_14nm_New_uArch.pdf
- [31] ITRS. (2013). *Process Integration, Devices, And Structures*. [Online]. Available: <http://www.itrs2.net/2013-itrs.html>
- [32] *International Technology Roadmap for Semiconductors*, document 32, 2010.
- [33] *FLUOstar Omega (Filter-Based Multi-Mode Microplate Reader), Gemini EM Microplate Reader*. [Online]. Available: <http://www.bmglabtech.com/en/products/omega-series/fluostar-omega/>
- [34] M. S. Alexander, *Plasmonics: Fundamentals and Applications*. New York, NY, USA: Springer, 2007.
- [35] N. Fang, H. Lee, C. Sun, and X. Zhang, "Sub-diffraction-limited optical imaging with a silver superlens," *Science*, vol. 308, pp. 534–537, Apr. 2005.
- [36] L. Zhou, F. Ding, H. Chen, W. Ding, W. Zhang, and S. Y. Chou, "Enhancement of immunoassay's fluorescence and detection sensitivity using three-dimensional plasmonic nano-antenna-dots array," *Anal. Chem.*, vol. 84, no. 10, pp. 4489–4495, 2012.
- [37] R. F. Oulton, V. J. Sorger, D. A. Genov, D. F. P. Pile, and X. Zhang, "A hybrid plasmonic waveguide for subwavelength confinement and long-range propagation," *Nature Photon.*, vol. 2, no. 8, pp. 496–500, Aug. 2008.
- [38] T. W. Ebbesen, H. J. Lezec, H. F. Ghaemi, T. Thio, and P. A. Wolf, "Extraordinary optical transmission through sub-wavelength hole arrays," *Nature*, vol. 391, pp. 667–669, Feb. 1998.
- [39] J. B. Pendry, "Negative refraction makes a perfect lens," *Phys. Rev. Lett.*, vol. 85, no. 18, pp. 3966–3969, Oct. 2000.
- [40] W. L. Barnes, A. Dereux, and T. W. Ebbesen, "Surface plasmon subwavelength optics," *Nature*, vol. 424, no. 6950, pp. 824–830, 2003.
- [41] R. Mehfuz, F. A. Chowdhury, and K. J. Chau, "Imaging slit-coupled surface plasmon polaritons using conventional optical microscopy," *Opt. Exp.*, vol. 20, no. 10, pp. 10526–10537, 2012.
- [42] X. Lu, L. Hong, and K. Sengupta, "An integrated optical physically unclonable function using process-sensitive sub-wavelength photonic crystals in 65 nm CMOS," in *IEEE ISSCC Dig. Tech. Papers*, Feb. 2017, pp. 272–273.
- [43] L. Hong and K. Sengupta, "Fully integrated optical spectrometer with 500-to-830 nm range in 65 nm CMOS," in *IEEE ISSCC Dig. Tech. Papers*, Feb. 2017, pp. 462–463.
- [44] L. Hong and K. Sengupta, "CMOS-based fluorescence biosensor with integrated nanoplasmonic filters," in *Proc. CLEO*, May 2017, pp. 1–2.
- [45] X. Wu and K. Sengupta, "On-chip THz spectroscope exploiting electromagnetic scattering with multi-port antenna," *IEEE J. Solid-State Circuits*, vol. 51, no. 12, pp. 3049–3062, Dec. 2016.
- [46] X. Wu and K. Sengupta, "A 40-to-330 GHz synthesizer-free THz spectroscope-on-chip exploiting electromagnetic scattering," in *IEEE ISSCC Dig. Tech. Papers*, Feb. 2016, pp. 428–429.
- [47] A. Hryciw, Y. C. Jun, and M. L. Brongersma, "Plasmonics: Electrifying plasmonics on silicon," *Nature Mater.*, vol. 9, pp. 3–4, Sep. 2010.
- [48] L. Tang, S. Latif, and D. A. B. Miller, "Plasmonic device in silicon CMOS," *Electron. Lett.*, vol. 45, no. 13, pp. 706–708, Jun. 2009.
- [49] H. M. G. Wassel *et al.*, "Opportunities and challenges of using plasmonic components in nanophotonic architectures," *IEEE J. Emerg. Sel. Topics Circuits Syst.*, vol. 2, no. 2, pp. 154–168, Jun. 2012.
- [50] D. Y. Fedyanin, D. I. Yakubovsky, R. V. Kirtaev, and V. S. Volkov, "Ultralow-loss CMOS copper plasmonic waveguides," *Nano Lett.*, vol. 16, pp. 362–366, Apr. 2016.
- [51] U. Resch-Genger, M. Grabolle, S. Cavaliere-Jaricot, R. Nitschke, and T. Nann, "Quantum dots versus organic dyes as fluorescent labels," *Nature Methods*, vol. 5, pp. 763–775, Apr. 2008.
- [52] *Qdot 800 Probe*. [Online]. Available: <https://www.thermofisher.com/us/en/home/life-science/cell-analysis/fluorophores/qdot-800.html>
- [53] D. Marc, P. Abshire, and E. Smela, "Optical filtering technologies for integrated fluorescence sensors," *Lab Chip*, vol. 7, no. 8, pp. 955–977, 2007.
- [54] E. Ozbay, "Plasmonics: Merging photonics and electronics at nanoscale dimensions," *Science*, vol. 311, no. 5758, pp. 189–193, Jan. 2006.
- [55] H. J. Lezec *et al.*, "Beaming light from a subwavelength aperture," *Science*, vol. 297, no. 5582, pp. 820–822, Aug. 2002.
- [56] F. J. Garcia-Vidal, L. Martin-Moreno, T. W. Ebbesen, and L. Kuipers, "Light passing through subwavelength apertures," *Rev. Mod. Phys.*, vol. 82, pp. 729–787, Apr. 2010.

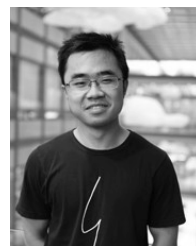
- [57] N. C. Lindquist, P. Nagpal, K. M. McPeak, D. J. Norris, and S.-H. Oh, "Engineering metallic nanostructures for plasmonics and nanophotonics," *Rep. Progr. Phys. Phys. Soc.*, vol. 75, no. 3, pp. 1–61, 2012.
- [58] S. Yokogawa, S. P. Burgos, and H. A. Atwater, "Plasmonic color filters for CMOS image sensor applications," *Nano Lett.*, vol. 12, pp. 4349–4354, Sep. 2012.
- [59] Q. Chen *et al.*, "A CMOS image sensor integrated with plasmonic colour filters," *Plasmonic*, vol. 7, no. 4, pp. 695–699, 2012.
- [60] E. D. Palik, *Handbook of Optical Constants of Solids*. San Diego, CA, USA: Academic, 1998.
- [61] W. Lukosz and R. E. Kunz, "Light emission by magnetic and electric dipoles close to a plane dielectric interface. II. Radiation patterns of perpendicular oriented dipoles," *J. Opt. Soc. Amer.*, vol. 67, pp. 1615–1619, Sep. 1977.
- [62] W. Lukosz, "Light emission by magnetic and electric dipoles close to a plane dielectric interface. III. Radiation patterns of dipoles with arbitrary orientation," *J. Opt. Soc. Amer.*, vol. 69, no. 11, pp. 1495–1503, 1979.
- [63] K. Murari, R. Etienne-Cummings, N. V. Thakor, and G. Cauwenberghs, "A CMOS in-pixel CTIA high-sensitivity fluorescence imager," *IEEE Trans. Biomed. Circuits Syst.*, vol. 5, no. 5, pp. 449–458, Oct. 2011.
- [64] M. Beiderman, T. Tam, A. Fish, G. A. Jullien, and O. Yadid-Pecht, "A low-light CMOS contact imager with an emission filter for biosensing applications," *IEEE Trans. Biomed. Circuits Syst.*, vol. 2, no. 3, pp. 193–203, Sep. 2008.
- [65] D. Ho, M. O. Noor, U. J. Krull, G. Gulak, and R. Genov, "CMOS spectrally-multiplexed FRET-on-a-chip for DNA analysis," *IEEE Trans. Biomed. Circuits Syst.*, vol. 7, no. 5, pp. 643–654, Oct. 2013.
- [66] M. W. Seo *et al.*, "A 10 ps time-resolution CMOS image sensor with two-tap true-CDS lock-in pixels for fluorescence lifetime imaging," *IEEE J. Solid-State Circuits*, vol. 51, no. 1, pp. 141–154, Jan. 2016.



Lingyu Hong received the B.S. degree in physics from Peking University, Beijing, China, in 2012.

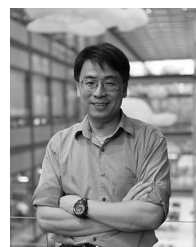
In 2013, he joined Prof. Sengupta's lab at Princeton University. His current research interests include the study, research, and implementation of interdisciplinary knowledge in photonics, electronics, and others for lab-on-chip systems, specifically for biomedical applications.

Mr. Hong was a recipient of the Analog Device Outstanding Student Designer Award in 2015, the Qualcomm Innovation Fellowship in 2015, and Circuits Society Pre-doctoral Achievement Award in 2017, and Qualcomm Innovation Finalist in 2017. He received the Peking University Academic Excellence Reward and various scholarships for his research in nanophotonics and plasmonics.



Hao Li received the B.Sc. degree in chemistry from Nanjing University, Nanjing, China, in 2013. He is currently pursuing the Ph.D. degree with Princeton University, Princeton, NJ, USA, under the supervision of Prof. H. Yang.

His current research interests include single-molecule protein dynamics.



Haw Yang received the B.S. degree from National Taiwan University, Taipei, Taiwan, and the Ph.D. degree from the University of California (UC), Berkeley, CA, USA.

He was a Post-Doctoral Fellow at Harvard, Cambridge, MA, USA, for two and half years. In 2002, he joined UC Berkeley and then moved to Princeton University, Princeton, NJ, USA, in 2009. He is currently a Professor of Chemistry with Princeton University. He is with the Yang lab, Princeton University, where he is involved in research in the chemical dynamics in complex systems, crosscutting the conventional fields of physical chemistry, chemical and materials biology, and biophysics.

Dr. Yang is a fellow of the Royal Society of Chemistry, a founding Associate Editor of *Chemical Science*, and on several Editorial Advisory Boards.



Kaushik Sengupta (M'12) received the B.Tech. and M.Tech. degrees in electronics and electrical communication engineering from IIT Kharagpur, Kharagpur, India, in 2007, and the M.S. and Ph.D. degrees in electrical engineering from the California Institute of Technology (Caltech), Pasadena, CA, USA, in 2008 and 2012, respectively.

In 2005, he joined the University of Southern California, Los Angeles, CA, USA, and then joined the Massachusetts Institute of Technology, Cambridge, MA, USA, in 2006, where he was involved in nonlinear integrated systems for high-purity signal generation and low-power RF identification tags. In 2013, he joined the Department of Electrical Engineering, Princeton University, Princeton, NJ, USA, as a Faculty Member. His current research interests include high-frequency ICs, electromagnetics, and optics for various applications in sensing, imaging, and high-speed communication.

Dr. Sengupta received the Young Investigator Program Award from the Office of Naval Research in 2017, and the Charles Wilts Prize in 2013 from the Department of Electrical Engineering, Caltech, for outstanding independent research in electrical engineering leading to a Ph.D. He was a recipient of the IBM Ph.D. Fellowship from 2011 to 2012, the IEEE Solid State Circuits Society Predoctoral Achievement Award in 2012, the IEEE Microwave Theory and Techniques Graduate Fellowship in 2012, the Analog Devices Outstanding Student Designer Award in 2011, the Prime Minister Gold Medal Award of IIT Kharagpur in 2007, the Caltech Institute Fellowship, the Most Innovative Student Project Award of the Indian National Academy of Engineering in 2007, and the IEEE Microwave Theory and Techniques Undergraduate Fellowship in 2006. He serves on the Technical Program Committee of the European Solid-State Circuits Conference and the Custom Integrated Circuits Conference. He was selected to the Princeton Engineering Commendation List for Outstanding Teaching in 2014 in 2016. He was a co-recipient of the IEEE RFIC Symposium Best Student Paper Award in 2012 and the 2015 IEEE MTT-S Microwave Prize.